

BIOINSPIRED DESIGN

BY

**OWOSEN, TUNJI ADETAYO**

A THESIS

SUBMITTED TO THE AFRICAN UNIVERSITY OF SCIENCE AND TECHNOLOGY

ABUJA – NIGERIA

IN PARTIAL FULFILLMENT OF THE REQUIREMENTS FOR THE

AWARD OF MASTER OF SCIENCE IN (MATERIALS SCIENCE AND ENGINEERING)

SUPERVISOR: **PROF. W. O. SOBOYEJO**

MAY 2013

BIOINSPIRED DESIGN

A THESIS APPROVED

BY

SUPERVISOR: **PROF. W. O. SOBOYEJO**

MEMBER \_\_\_\_\_

NAME

MEMBER \_\_\_\_\_

NAME

*With love,*

*this work is dedicated to all seekers of knowledge, sincere tutors, supporters of truth, as  
well as caring and committed parents*

## Acknowledgements

All praise is due to the Almighty God, the uncreated creator, the Lord of the Worlds. It is He alone that I worship and it is from Him that I seek help. He is the Creator of souls, the Guider of hearts, and the Master of the Day of Judgment. I would not be here today without His blessings, favours, grace, and sustenance. Thank you my Lord.

My sincere gratitude goes to my advisor, **Prof. Wole Soboyejo**. I found in him a mentor who has not only guided me through this work, but also motivated me to do more. His painstaking review of my write-ups would for all time live in my memory. My meeting you is not a chance it is the design of God. I have got no big purse but my heart is large, please accept my unalloyed appreciation. Thank you.

Engr. Tawfeeq Agbaje, Mr. Ilyas Agboola, Mr. Adam Sulaiman, Dr. Omololu Akin-Ojo, and a host of other well wishers and supporters, to you all I say may your leaves be green. Adeleke Fatimah (Mrs.) has not just been a friend, her all time call kept me aloft when I could have been down. My Olukemi's words and supplications were in no small measure usefull. To her I say 'jazaakillahu khairan!' The Jaji's, the Oyedele's, and the Mahmud's, all of Sunny Vale Estate, Abuja make my stay in Abuja worthwhile. Your children for whom we met, I pray will live to always make you happy.

I would like to thank specifically, Idris Adaviriku Malik (Petroleum Engineering AUST), Elijah Ericmore Jossou (Materials Science and Engineering, AUST), Dr. A. Alarape, Dr. A. Omonona (Mrs.) (both of Fisheries and Wild Life Management Department, University of Ibadan), and Dr. S. G. Olukole (Veterinary Anatomy Department, University of Ibadan) for their unique contribution to the successfull completion of this work.

I must also thank all those who made my labouratory work and experience wholesome, Dr. Zebaze Kana, Dr. Shola Odusanya, Mr. Gadu Ibrahim, IT students, all of Sheda Science and Technology Complex, Abuja, please accept my unreserved appreciation.

My gratitude further goes to my friends, students, staff and professors, here at African University of Science and Technology, Abuja, especially members of the Muslim

Community. The experience has been great and thank you all for an amazing eighteen months. If I could, I would mention all of you by names but my relationship with each of you is unique and cannot be expressed in simple words.

My thesis would be incomplete without the mention and expression of profound gratitude to my bosom friend, Adeniji Sharafadeen Adetunji, with whom the journey began. Thank you for being there when I needed you most.

I express my unalloyed gratitude to my parents **Mr. and Mrs. Owoseni**, and my siblings especially Abu Mardhiyyah, who through all odds stood by me to ensure that I do not lose focus and in the end achieve this feat. They have always been there for me in every aspect of my life. This thesis is indeed for the family.

It will for all times be in my heart the part played by Muslim Students' Society of Nigeria (**MSSN**) **University of Ibadan** in the development of my person. To the Society that made me, I say may her leaves be green!

This research would not have been possible without the AUST/ADB funding and the Nelson Mandela Institution (NMI). I am grateful to these organizations for their financial support.

To everyone, may The Good God of Creations be your guard and guide. Aameen!

Is there any reward for good, than good? (Q55: 60)

## **Abstract**

Bioinspired design involves the use of concepts observed in natural biological materials in engineering design. The hope is that the leveraging of biological materials in the engineering domain can lead to many technological innovations and novel products. This work presents the initial material characterization of *kinixys erosa* tortoise shell using a combination of x-ray diffraction, optical/scanning electron microscopy and micro-mechanical testing. The results were used in the analytical/computational modelling of shell structures. The potential implications of the results were then discussed to give fundamental understanding of deformation and stress responses of shell structures.

# Table of Contents

Acknowledgments.....	iv
Abstract.....	vi
Table of Contents.....	vii
List of Figures.....	ix
List of Tables.....	xii
1 BACKGROUND AND INTRODUCTION .....	1
1.1 Background and Motivation .....	1
1.2 Unresolved Issues .....	2
1.3 Objective and Scope of Thesis Work.....	2
References	
2 LITERATURE SURVEY .....	5
2.1 Introduction.....	5
2.2 Biological Materials: Microstructural, Compositional, and Mechanical Characterization .....	5
2.3 State of the Art in Biomimetics .....	17
2.4 Bioinspired Design Approaches .....	18
References	
3 CHARACTERIZATION OF THE MULTI-SCALE STRUCTURE OF KINIXYS EROSA SHELL .....	37
3.1 Introduction.....	37
3.2 The Structure of a Typical Tortoise Shell .....	37
3.3 Bone Structure .....	38
3.4 Experimental Methods .....	38
3.5 Results and Discussion .....	39
3.6 Summary .....	42
References	

4	ANALYTICAL AND COMPUTATIONAL MODEL OF MULTI-LAYERED SHELL STRUCTURE .....	50
4.1	Introduction.....	50
4.2	Analytical Model Based on Theory of Shell .....	50
4.3	Computational Finite Element Model .....	51
4.4	Results and Discussion .....	52
4.5	Summary .....	54
	References	
5	CONCLUDING REMARKS AND SUGGESTED FUTURE WORK .....	64
5.1	Summary and Concluding Remarks .....	64
5.2	Implications and Possible Bioinspired Applications .....	64
5.3	Suggestions for Future Work.....	64
	References	
	Appendix A	
	Appendix B	

## List of Figures

Figure 2.1: Multiscale hierarchy and structure of the turtle shell .....	22
Figure 2.2: Chemical analysis results obtained from different surfaces of the turtle shell carapace.....	23
Figure 2.3: Microstructure of the turtle shell of <i>Trachemys scripta</i> .....	24
Figure 2.4: Cross-sectional of the <i>Chelydra serpentina</i> 's carapace .....	24
Fig. 2.5: (a) X-ray diffraction pattern eliciting diffused hydroxyapatite (HA) peak and (b) Raman spectrum showing presence of amorphous top surface and calcium-phosphate in the bottom surface of the turtle's carapace .....	25
Figure 2.6: Cross-sectional SEM image of (a) Turtle's carapace, and elemental mapping of (b) carbon, (c) phosphorous, and (d) calcium eliciting the presence of carbon fibers in the calcium phosphate matrix .....	26
Figure 2.7: Indentation test results obtained from (a) nano-indentation and (b) Vickers hardness tests on the side surface of the turtle shell carapace .....	26
Figure 2.8: Stress/strain curves from the quasi-static compression test results on the turtle shell carapace coupon specimens under various strain rates and specimen geometries.....	27
Figure 2.9: Comparison of three-point bending test results obtained from actual data and ABAQUS finite element simulations; (a) without considering foam material effect, and (b) considering foam material effect .....	27
Figure 2.10: Load-displacement curve of Compression failure tests of Ts shell.....	28
Figure 2.11: Tensile stress-strain curves at different locations of the shell.....	29
Figure 2.12. The fiber beams enhancing the thin composite film located on the inside surface .....	29
Figure 2.13: Load indentation-depth profile of the various layers, with the main image showing the structural rigid dense 3rd layer and matrix, and the inset showing a zoomed image of the dotted box for the top layer, waxy 2nd layer, and the two carbonaceous lamellae/fibrous 4th and 5th layers of the turtle's carapace .....	30
Figure 2.14: Schematics of (a) the samples prepared from bamboo and (b) cross-section of the samples and nanoindentation matrix.....	31
Figure 2.15: (a) A schematic of the dog bone tensile test sample. (b) A schematic of microtensile sample locations (samples are fabricated along the fiber orientations).....	31

Figure 2.16: (a) Schematics of the four point bending sample from the outside, inside and side crack orientations. (b) A schematic of the experimental set-up and beam cross-section for the four point bending experiment .....	32
Figure 2.17: The Young’s moduli distribution along the radial direction of the bamboo cross-section .....	32
Figure 2.18: An optical image of the functionally graded mesostructure of bamboo .....	33
Figure 2.19: (a) A representative stress–strain curve for the bamboo microtensile experiment. (b) Tensile strength of the outside, side and inside specimens .....	33
Figure 2.20: Crack growth for moso culm bamboo. (a) SEM image of cellulose bridging in the outside crack SENB sample. (b) SEM image of ligament bridging in the side crack SENB sample .....	34
Figure 2.21: (a) An ABAQUS deformed finite element mesh for the symmetrical SENB crack model during the four point bending test. (b) The stress concentration contour around the crack tip under the registered loads and crack lengths .....	34
Figure 2.22: Resistance curve results for moso culm bamboo .....	35
Figure 2.23: Journals and conferences publishing research on biomimetics.....	35
Figure 3.1: Carapace [C] and Plastron [P] of kinixys erosa .....	44
Figure 3.2: Scutes on the carapace of kinixys erosa tortoise shell.....	45
Figure 3.3: Cross section of kinixys erosa bone structure .....	45
Figure 3.4: Schematic of kinixys erosa bone structure .....	45
Figure 3.5: X-ray spectrum of kinixys erosa shell bone .....	46
Figure 3.6: X-ray spectrum of kinixys erosa scute .....	46
Figure 3.7: Stress-strain plot of compression test on kinixys erosa carapace bone structure ..	47
Figure 3.8: Load/deformation plot three point flexural test on kinixys erosa carapace bone structure.....	47
Figure 3.9: Compression test samples .....	47
Figure 3.10: Bend test samples .....	47
Figure 3.11: Schematic of bend test sample .....	48
Figure 3.12: Schematic of compression test sample.....	48
Figure 3.13: Load indentation-depth profile of the cortical layer of the multilayered carapace bone of Ke tortoise shell .....	49
Figure 4.1: Stress distribution along the surface of the shell.....	55

Figure 4.2: Strain distribution along the surface of the shell.....	56
Figure 4.3: Tangential strain distribution along the surface of the shell .....	56
Figure 4.4: Radial strain distribution along the surface of the shell .....	57
Figure 4.5: Deformation distribution along the surface of the shell.....	57
Figure 4.6: Tangential deformation distribution along the surface of the shell.....	58
Figure 4.7: Radial deformation distribution along the surface of the shell .....	58
Figure 4.8: Loaded 2-D finite element model of the shell structure.....	60
Figure 4.9: 2-D Finite element model showing stress distribution along the surface of the shell (undeformed) .....	60
Figure 4.10: 2-D Finite element model showing stress distribution along the surface of the shell (deformed) .....	61
Figure 4.11: Loaded 3-D finite element model of the dome structure .....	61
Figure 4.12: Meshed 3-D finite element model of the dome structure (undeformed) .....	62
Figure 4.13: 3-D Finite element model showing stress distribution on the surface of the dome structure (deformed single/multilayer) .....	62
Figure 4.14: 3-D Finite element model showing stress distribution on the surface of the dome structure (deformed multilayer) .....	63
Figure 4.15: 3-D Finite element model showing stress distribution on the surface of the dome structure (deformed single layer) .....	63

## List of Tables

Table 2.1: Finite element simulation conditions.....	27
Table 2.2: The tensile modulus and strength of Tc shell materials .....	28
Table 2.3: The elastic modulus and ultimate strength of Tc strengthen rib.....	28
Table 2.4: Construct of the layered structure in a turtle shell with consequent mechanical properties of each layer .....	30
Table 2.5: Leading journals publishing research on biomimetics .....	36
Table 2.6: Leading conferences publishing research on biomimetics .....	36
Table 2.7: Leading conferences publishing research on biomimetics .....	36
Table 3.1: Load-displacement data of flexural test on kinixys erosa bone structure.....	48
Table 4.1: Analytical solutions based on theory of shell .....	55
Table 4.2: Finite element simulation conditions.....	59
Table 4.3: 3-D Finite element simulation conditions.....	59

## **1.0 Background and Introduction**

### **1.1 Background and Motivation**

Bioinspired design involves the use of concepts observed in natural biological materials in engineering design. The hope is that the leveraging of biological materials in the engineering domain can lead to many technological innovations and novel products [1]. Similarly, the field of Biomimetics involves the imitation of nature [2]. It is a multidisciplinary field that can also result in the development of novel materials with remarkable mechanical properties.

Many biological tissues and devices have remarkable engineering properties [3]. For example, the toughness of spider silk [3], the specific strength and stiffness of bamboo [3] or the adhesion abilities of the gecko feet [3] are a few of the many examples of high-performance natural materials [3, 4].

Unlike the design of conventional engineering materials that often involve the use of multiple materials chemistries in the design of engineering components and systems, natural biological materials are made from relatively few chemical constituents. For example, a molecule such as type I collagen serves as the building block for a variety of tissues in the human body. These include: bone; cartilage; skin and the cornea in the eye.

In many cases, hard biological materials exist as composites. These high-performance natural composites are made up of relatively weak components (brittle minerals and soft proteins) arranged in intricate ways to achieve specific combinations of stiffness, strength and fracture toughness (resistance to cracking). Determining which features control the performance of biological materials is the first step in Biomimetics. These 'key features' can then be implemented into artificial bio-inspired synthetic materials, using innovative techniques such as layer-by-layer assembly of nanocomposites [2] or ice-templated crystallization or freeze casting [6, 7].

In their work entitled “Biological Materials: Structure and Mechanical Properties” Meyers et al. [5] studied several biological materials (e.g. nacre, ligaments, hoofs, blood vessels, beak interiors, chameleon, etc.) using diverse materials approaches. Scanning Electron Microscopy (SEM), Transmission Electron Microscopy (TEM), Atomic Force Microscopy (AFM), nanoindentation, and molecular simulations and modelling were used to study the layered structures and their hierarchy, multi-functionality, and self-healing capabilities. The various building blocks were also linked to their remarkable mechanical properties.

## **1.2 Unresolved Issues**

Although there have been several studies of biological materials, there have been only limited studies of the shell structure of tortoise shells [8 - 11]. Prior work by Chenzhao et al [8], Rhee et al [9], Kantesh et al [10], and Magwene, P. M. and Socha, J. J. [11] have studied the microstructure and mechanical property of different species of turtle. Even so, the turtle shell carapace possesses superior armour behaviour against environmental threats [9], there have not been detailed studies of the effects of shell structure on their mechanical properties. There have also been few studies that have tried to apply shell theory [12] to the bioinspired design of materials and structures. These will be explored in this study using a combination of experiments and analytical/computational models.

## **1.3 Objective and Scope of Thesis Work**

### **1.31 Objective**

The objective of this thesis is to develop a fundamental understanding of the deformation and stress responses of a *Kinixys erosa* tortoise shell structure as a potential source of inspiration for the design of a failure resistant shell/layered structure.

### 1.32 Scope

This thesis presents a combination of experimental, theoretical and computational studies of the structure and mechanical properties of kinixys erosa tortoise shell structures. These are studied as potential sources of bioinspiration for the design of shell structures that are resistant to bending. The thesis is divided into five sections. Following the introduction and background (Chapter 1), a review of relevant literature is presented in Chapter 2. A characterization of the multi-scale structure of the kinixys erosa shell is then elucidated along with the basic mechanical properties in Chapter 3. Selected examples of potential shell structures that are inspired by the ideas presented in this thesis are then presented in Chapter 4, via analytical and computational models. The salient conclusions arising from this work are then summarized in Chapter 5 along with some suggestions for future work.

### References

1. **Abdulkadir, E.** 2010. *BioMimetic/BioInspired Robots and Mechatronics Engineering Design*. PowerPoint Presentation at Department of Mechatronics Engineering Atılım University Ankara, Turkey. Accessed 18 June 2012, 03:53 p.m.
2. **Barthelat, F.** 2007. *Biomimetics for Next Generation Materials*. *Phil. Trans. R. Soc. A* 365, 2907–2919 (doi:10.1098/rsta.2007.0006).
3. **Jackson, A. P., Vincent, J. F. V. & Turner, R. M.** 1988. *The Mechanical Design of Nacre*. *Proc. R. Soc. B* 234,415–440 (doi:10.1098/rspb.1988.0056)
4. **Sanchez, C., Arribart, H. & Giraud Guille, M. M.** 2005. *Biomimetism and Bioinspiration as Tools for the Design of Innovative Materials and Systems*. *Nat. Mater.* 4, 277–288.
5. **Meyers, M. A., Chen, P. Albert, Y. L., Yasuaki, S.** 2008. *Biological Materials: Structure and Mechanical Properties*. *Progress in Materials Science*. 53, pp. 1-206.
6. **Munch, E., Launey, M. E., Alsem, D. H., Saiz, E., Tomsia, A. P., Ritchie R. O.** 2008. *Tough, Bio-inspired Hybrid Materials*. *Science* Vol. 322 no. 5907 pp. 1516-1520 doi: 10.1126/science.1164865.

7. **Niu, X., Rahbar, N., Farias, S., Soboyejo, W.** 2009. *Bio-inspired Design of Dental Multilayers: Experiments and model.* JMBBM Vol. 2 issues 6 pp. 596-602.
8. **Wei Z., Chengwei W., Chenzhao Z.\*, and Zhen C.** *Microstructure and mechanical property of turtle shell.* : The Chinese Society of Theoretical and Applied Mechanics, 2012, Theoretical & Applied Mechanics Letters 2.
9. **Rhee, H., Horstemeyer, M. F., Hwang, Y., Lim, H., El Kadiri, H., Trim, W.** *A study on the structure and mechanical behavior of the Terrapene carolina carapace: A pathway to design bio-inspired synthetic composites.* s.l. : Elsevier, 2009, Materials Science and Engineering C, pp. 2333-2339.
10. **Kantesh, B., Riken, R. P., Anup, K. K., Debrupa, L., Arvind, A.** *Multi-scale hierarchy of Chelydra serpentina: Microstructure and mechanical properties of turtle shell.* s.l. : Elsevier, 2011, Journal of the Mechanical Behavior of Biomedical Materials, Vol. 4, pp. 1440-1451.
11. **Magwene, P. M., Socha, J. J.** *Biomechanics of turtle shells: How whole shells fail in compression.* 2012. J. Exp. Zool. 9999A:1 – 13.
12. **Stephen T. and Woinowsky-Krieger S.** *Theory of Plates and Shells.* Singapore : McGraw-Hill, Inc., 1959. 0-07-085820-9.

## **2.0 Literature Survey**

### **2.1 Introduction**

The design field is often designated by its end products e.g. mechanical design, electrical design, building design, etc [1]. Furthermore, there are basically three approaches to design. These include traditional design, design optimization, and axiomatic design [1]. If then, solutions to problems must start from what is known, can there be novel solutions [2]?

By definition, bioinspired design (BID) is based on cross domain analogies [2]. BID is a growing field that is driven partly by the desire for eco-friendly solutions [2]. On the other hand, the fast changing world we inhabit brings up novel challenges that require unique engineering solutions that cannot be easily imitated [3]. This quest for novel solutions and creativity has stimulated the study of natural materials for alternative insight into how to address a number of societal challenges. The natural materials so studied are called biological materials [4].

BID has influenced many engineering disciplines [5]. For example plant and insects have inspired engineering designs in recent times [6] e.g. unmanned air vehicles that imitate the articulated wings of insects [7] and birds or the motion detection systems inspired by the compound vision systems of insects [8] amongst others. This chapter presents an overview of prior work on biological materials and bioinspired design.

### **2.2 Biological Materials: Microstructural, Compositional, and Mechanical Characterization**

#### **2.21 Microstructural and Compositional Characterization of Turtle Shells**

Rhee et al. [9] investigated the multiscale structure of *Terrapene carolina* carapace (Tc) using optical microscopy and scanning electron microscope (SEM). Samples were prepared from the carapace using a diamond saw. These were cleaned with an ultrasonic cleaner. A cold mounting

technique was used to mount the samples with epoxy. These were then studied in a SUPRA-40 field emission gun (FEG)-SEM (CarlZeiss SMT Ltd, Cambridge, United Kingdom). Energy dispersive X-ray (EDX) spectroscopy technique was used to ascertain the chemical composition of Tc shell during SEM.

The results obtained showed that the shell is a multiphase composite material arranged by a multiscale hierarchy, as shown in Figure 2.1. Chemical analysis of the shell material (Figures 2.2 (a) – (c)) revealed that the keratin layer is made of carbon (C), oxygen (O), nitrogen (N), and sulphur (S) which are proteinous elements. On the other hand, the underlying layer to the scute was found to contain minerals based on the detected constituent elements: calcium (Ca, 15–20 wt.%), phosphorous (P, 7–10 wt.%), sodium (Na), chlorine (Cl) and magnesium (Mg).

In the work of Chenzhao et al. [10] on *Trachemys scripta* (Red-ear turtle) found in Southern China, the microstructural analysis revealed a structure that is similar to *Terrapene carolina* (Tc), as shown in Figures 2.3 (a) – (f). They also showed that its shell is a multiphase composite material with 0° layered architecture.

Balani et al. [11] worked on the freshwater snapping turtle, *Chelydra serpentina* (Cs). Microstructural- and compositional analyses of Cs carried out using field emission scanning electron microscopy (SEM) (FESEM JEOL JSM 6330F, JEOL 5900 LV SEM, Siemen's D-500, Munich, Germany). Their results revealed that Cs carapace is a multi-layered structure, as shown in Figures 2.4 (a) – (d). It has a waxy 10–15 µm thick top external exocortical bone underlined by a thin (5–10 µm) semi-waxy internal endocortical layer Figure 2.4 (b). The third layer is a highly dense cortical bone tissue (~ 50 µm thick) that shows a minor crack along the interface with adjacent layers Figures 2.4 (b) and (c). The fourth and fifth layers are two lamellae-type bone layers that are ~ 175 µm and ~ 75 µm thick, respectively. These last two layers appear similar in morphology with respect to each other, but the former is much more loosely packed in comparison to latter. The turtle's carapace was found to consist of a matrix (~ 3000 µm thick) containing a highly porous (~ 50% – 60%) cancellous bone tissue. This has an effect on the toughness of the turtle shell, serving as the structural material for load bearing. This structure

enables the turtle to swim fast and manoeuvre, while it provides resistance to bending and high stiffness.

The trio of X-ray diffraction, Raman spectroscopy, and EDX elemental mapping confirmed the presence of carbonaceous top surface and a calcium phosphate matrix (Figures 2.5 (a) and (b)). Furthermore, the pores in the calcium phosphate matrix were found to be reinforced with a fibrous structure (Figure 2.6 (a)). The structure reveals a fibre reinforced composite designed by nature to toughen the calcium phosphate matrix (Figures 2.6 (c) and (d)). The presence of carbonaceous fibres in the pores of matrix suggests additional strengthening of the calcium phosphate matrix in the turtle's carapace.

## **2.22 Mechanical Characterization of Turtle Shell**

Rhee et al. [9] have studied the mechanical properties of Tc shell using nano- and micro-indentations, quasi-static compression and bending tests. The nanoindentation tests were carried out using a Hysitron TriboIndenter® (Hysitron, Minneapolis, MN ) at ambient temperature. The indents were obtained using a Berkovich type indenter that was used under load control. The loading included a 20 s monotonic loading segment, a 2 s constant-load holding time, and a 20 s unloading segment. The loading and unloading rates of such tests were 450  $\mu\text{N/s}$ .

To obtain global information on the side surfaces of the carapace of the turtle shell, micro-indentation tests were conducted using a LMV Series 50V LECO Vickers hardness tester (LECO Corporation, MI, USA). The tests were conducted with a pyramidal diamond tip and a load of 25 gf. at ambient temperature. Quasi-static compression tests carried out using Instron 5882 electromechanical test machine with a maximum load capacity of 100 kN. The tests were performed on specimens fabricated according to ASTM D790. These were cut in the longitudinal and transverse directions of Tc shell carapace. The cut specimens were tested at room temperature with strain rates ranging from  $10^{-4}$  to  $10^0 \text{ s}^{-1}$ .

The bending strengths of the Tc carapace material were obtained via three-point bend testing in a Model 5882 Instron electromechanical testing machine (Instron, Norwood, MA, USA). The tests were conducted at room temperature with a cross-head speed of 0.5 mm/min. A linear variable displacement transducer (LVDT) was used to measure the induced displacement. The local strain histories at specific locations were also obtained from foil strain gauges that were attached to the top and bottom sides of the specimens. The NI-DAQmx software package (National Instruments, Newbury, United Kingdom) was used to analyse the recorded signals.

The nano- and micro-indentation tests on the side surfaces of the turtle shell carapace results presented in Figure 2.7. These reveal that the exterior layers and interior bony closed-cell walls possess comparable hardness and modulus values. The nano-indentation tests results gave Hardness and elastic moduli values ranging from 0.8 – 1.1 GPa and 18.3 – 24.8 GPa, respectively; while Vickers hardness tests yielded average hardness value of about Hv100 that corresponds to a strength of 0.98 GPa. The small variations in hardness and elastic modulus values from experimental results were attributed to specimen texture.

Two different types of coupon specimens were used for the quasi-static compression tests. The strain rate effect on the mechanical behavior of the turtle shell was compared to the varying density levels of the shell material, the results are as shown in Figure 2.8.

The three-point bend test on the rectangular specimens yielded data that were fitted into the following formulae:

$$\sigma = \frac{Mc}{I} = \left(\frac{FL}{4}\right) \left(\frac{d}{2}\right) \left(\frac{12}{bd^3}\right) = \frac{3FL}{2bd^2} \dots \dots \dots (1)$$

$$\varepsilon_f = \frac{6Dd}{L^2} \dots \dots \dots (2)$$

$$E_B = \frac{L^3 m}{4bd^3} \dots \dots \dots (3)$$

The above expressions were used to obtain: the flexural strength ( $\sigma_f$ ), flexural strain to failure ( $\epsilon_f$ ), and the Young's modulus in bending ( $E_B$ ), where  $M$  is the maximum bending moment,  $c$  is the distance from center of specimen to the outer fibers,  $I$  is the second moment of area of the cross-section,  $F$  is the applied load,  $L$  is the support span,  $d$  is the depth of test specimen,  $b$  is the width of test specimen,  $D$  is the maximum deflection of the specimen center, and  $m$  is the slope of the tangent to the initial straight line of the load deflection curve.

The stress - strain curve obtained from both the flexural tests data and the compression tests showed similar trends. The slope of the initial linear elastic deformation curve gave the Young's modulus.

Figures 2.9 (a) and (b) shows the comparisons between flexural test results obtained from the experimental data and FEA simulations using ABAQUS software. The FEA simulation conditions are as presented in Table 2.1 below. Only the FEA simulation results for a selected actual test condition of  $E_B = 7.1$  GPa are presented. In the region of initial elastic deformation, both single shell three-layer element and a discrete three-layer element were used in the FEA simulations. The initial simulations yielded much higher  $E_B$  values than that obtained from actual tests in both cases. Given that the effect of pores were not considered in the simulations, the FEA simulations' results resulted in much stiffer stress - strain responses than those from the experiments (Figure 2.9 (a)).

The FEA results exhibited much closer results, when the void volume fraction was considered (Figure 2.9 (b)). The overall material properties could be estimated using an equivalent inclusion idealization based on the void volume fraction in the turtle shell, which can then be adopted in the finite element model. By using modified material properties, the FEA simulation results gave better comparisons with experimental test results (Figure 2.9 (b)); the three-discrete layer approach captures strain reversal through-the-thickness direction, if the soft core material is located between hard face sheet materials like a sandwich structure. However, one single shell

element simulation through-the-thickness direction did not capture the strain reversal that occurred in the soft core material.

Chenzhao et al. [10] mechanically characterized both the shell and shell material of *Trachemys scripta* (Ts). The mechanical properties of Ts shell (length ~ 220 mm, width ~ 145 mm) were measured under varying loads. These were obtained by arranging the specimens between two parallel steel surfaces. The plates were then compressed at a compression speed of 2 mm/min. Figure 2.10 (a) shows also the corresponding force-displacement curve). The compression failure load for the shell was found to be ~ 3.33 KN corresponding to the maximum displacement (top board center) of 10.8 mm. There are four strengthening ribs connecting the shell top board and bottom plate. Under a compressive load, the ribs will be subjected to compression, and thus the four ribs look like four pillars to help supporting the top board. However, the turtle shell as a whole will be subjected to bending. Hence the inside surface is under tension, while the outmost surface is under compression.

The mechanical property of Ts shell material was measured by cutting the shell into three thin plate specimens (length = 40 mm, width = 5mm and thickness = 1 mm). Displacement was measured using electronic extensometer with a resolution 0.01 mm (YYU- 2520, New SANS Inc. in Shanghai, China).

The stress-strain relation obtained from the force-displacement curve is based on the engineering stress and strain definitions. These assume volume conservation.

$$\sigma = \sigma_{\text{eng}} (1 + \epsilon_{\text{eng}}) \quad (4)$$

$$\epsilon = \ln (1 + \epsilon_{\text{eng}}) \quad (5)$$

where  $\sigma$  is the true stress,  $\epsilon$  is the true strain,  $\sigma_{\text{eng}}$  is the engineering stress and  $\epsilon_{\text{eng}}$  is the engineering strain.

Figure 2.11 shows typical stress-strain curves for each layer of Ts shell material. Most layers (especially the interior layer) exhibited a little stiffened behaviour at the early stages of loading.

At small strains, the specimens were deformed in a linear elastic manner due to the cell wall deformation. Soon after the initial linear elastic deformation stage, failure of the cell walls occurs. The subsequent linear deformation is attributed to the effects of densification as observed by Rhee et al. [9] in the bending tests on Tc shell. Hence, the interior layer gives rise to the highest strength and modulus, while the middle layer has the lowest strength and modulus.

Tables 2.2 and 2.3 present the tensile modulus and strength of the Ts shell materials at different locations. The strength and modulus at other locations in the shell are obviously lower than at the strengthening rib. The corresponding modulus to small strains (less than 0.001) is considered as the initial modulus; the ratio of the fracture stress and the fracture strain gives the estimate of the final modulus (Figure 2.11 (b)). The latter is similar to the average tensile modulus. The inside surface of the shell, especially the bottom plate, is covered with a bio-fibre-reinforced thin film with a thickness of  $\sim 28$  microns (Figure 2.12). This special composite film yields the highest strength in the turtle shell, especially at the location that is closed to the strengthening rib. This is because it is believed that such a distribution of the bio-fibres may follow the stress direction on the inside surface of the bottom plate. This resists the evolution of cracking in the structure.

Ts shell can be divided into three layers (interior layer, exterior layer and middle layer) based on their strength. Their average tensile moduli are 500 MPa, 256 MPa and 230 MPa, while their tensile strengths are estimated at 40 MPa, 28 MPa and 19 MPa respectively. This layer of thin film material gives the highest strength in the turtle shell, reaching 98 MPa.

Nanomechanical characterization of Chelydra serpentine (Cs) by Balani et al. [11] revealed yet some other interesting information about turtle shell. Dry Cs carapace was subjected to nanoindentation using a Berkovich diamond indenter tip on a Hysitron TriboIndenter®. The instrument was calibrated using standard fused quartz and aluminium samples. The indenter tip used was a three-sided pyramidal type with an included angle of  $142.3^\circ$  and a tip radius of  $\sim 150$  nm. This was used to apply a maximum loads of 2000  $\mu\text{N}$  (ramp of 200  $\mu\text{N/s}$ ) and 100  $\mu\text{N}$  (ramp of 10  $\mu\text{N/s}$ ) for hard and soft regions of the samples, respectively.

The adjustment of the maximum load was automatic for a stipulated ramp load set for 10 s. To accommodate the neighbouring effect of the thin ( $\sim$  tens of  $\mu\text{m}$ ) and complex sandwich structure of turtle's carapace, the final displacement was between 50 – 300 nm. A dwell time of 10 s was applied to enable the relaxation of material prior to 10 s on unloading. The hardness values and the reduced moduli of the samples were computed automatically using the Oliver and Pharr method [12 - 16]. This was done by taking the elastic modulus and Poisson's ratio of the indenter to be 1141 GPa and 0.07 respectively. To extract the corresponding mechanical properties of each of the Cs carapace layers, an average of ten indentations were performed. It should be stated, however, that the choice of indenter tip and roughness of samples has influence on the elastic and plastic components of the load-indentation depth curves during indentation.

Figure 2.13 shows the load–displacement indentation curves of the various layers in the turtle's carapace. Trapezoidal load functions were used to prevent the effect of creep. High rates of unloading ( $10\text{--}200 \mu\text{N/s}$ ) were used to minimize the possible effects creep might have on the elastic modulus of the biological samples. The rigid dense layer was able to share the maximum load with minimal deformation with the matrix serving as the main structural material for load bearing, since it has the highest cross-sectional area with  $\sim 3 \text{ mm}$  thickness.

The top waxy layer and the carbonaceous lamellae/ fibrous layers are highly compliant ( $E$  of  $< \sim 2 \text{ GPa}$ ) with the second layer ( $E = 8.25 \text{ GPa}$ ,  $H = 208.3 \text{ MPa}$ ) which serves as a transition from the very soft waxy layer on the top surface ( $E = 2.03 \text{ GPa}$ ,  $H = 74.3 \text{ MPa}$ ) and to the rigid third layer ( $E = 22.15 \text{ GPa}$ ,  $H = 522.2 \text{ MPa}$ ). The subsequent underlying carbonaceous lamellae/fibrous layers are compliant ( $E < 1.5 \text{ GPa}$ ) and quite soft ( $H = 50 - 70 \text{ MPa}$ ). They can therefore serve as cushions to shield the structure from impacts. The inset shown in Figure 2.13 depicts the yielding effect of the fifth lamellar layer, seen in the sudden slipping (with extended depth) of the indenter during interaction with the layered structure as the sample was been loaded.

The high elasticity index ( $\sim 0.91$ ) of the soft carbonaceous lamellae/fibrous layer as presented in Table 2.4, was quite remarkable. This is such that the absorbed shock by the soft carbonaceous

layer can be recovered to 91% of its deformation instantly. This ensures structural support and the protection of the organs of Cs. The ventral portion of the turtle's carapace comprised a majority of the matrix, which is a rigid load-bearing scaffold ( $E = 11.34$  GPa,  $H = 253.4$  MPa). The porosity of the matrix also provides it with high impact resistance. Hence, the Cs carapace is a naturally evolved composite layer with proven multi-functionality (load bearing structure, tough and impact resistant casing, buoyancy and manoeuvrability, bending resistance, fluid reservoir).

The studies of the multilayered structure of Chelydra serpentine (Cs) therefore suggest that the sub-surface rigid layer provides much of the structural support and protection. The overall layered structure also appears to have a waxy top surface with a functionally graded structure. The moduli and hardness vary from the top layer ( $E = 2.03$  GPa,  $H = 74.3$  MPa), to the second layer ( $E = 8.25$  GPa,  $H = 208.3$  MPa), the third rigid layer ( $E = 22.15$  GPa,  $H = 522.2$  MPa), the cushioning carbonaceous lamellae layers ( $E < 1.5$  GPa,  $H < 100$  MPa), and finally to the structurally supporting matrix ( $E = 11.34$  GPa,  $H = 253.4$  MPa). This is a structure that provides basis for bioinspired design and bio-mimicking.

### **2.23 Mechanical Characterization of Functionally Graded Hierarchical Bamboo Structures**

Tan et al. [17] studied the mechanical properties of moso culm functionally graded bamboo structures using a combination of nanoindentation, micro-tensile testing, and resistance curve experiments. Young's moduli were measured across the polished cross-section of moso culm bamboo, via nanoindentation experiments. These were measured using a TriboScope Nanomechanical Testing System (Hysitron Inc., Minneapolis, MN) with a cube corner tip that was calibrated by performing nanoindentation tests on quartz, which exhibits size independent moduli. A 5 by 10 matrix was adopted for the nanoindentation geometry (Figure 2.14 (a) and (b)). The tests were performed under load control. Contact mode AFM scans were also obtained before and after each indentation point, in addition to the corresponding load-depth curves. The indentation process was such that a maximum force of 700  $\mu$ N was applied in 5 s, followed by a

dwelt time of 2 s and unloading for 5 s. Plots of load against displacement in the unloading region yielded the reduced moduli and hardness data. The hardness  $H$  and reduced moduli  $E_r$  were defined as

$$H = \frac{F_{max}}{A_p} \quad (6)$$

$$E_r = \frac{1}{\beta} \frac{\sqrt{\pi}}{2} \frac{1}{\sqrt{A_p}} \frac{dP}{dh} \quad (7)$$

where  $F_{max}$  is the maximum load,  $A_p$  is the projected contact area,  $\beta$  is a geometrical constant, which is 1.034 for a cube corner tip, and  $dP/dh$  is the initial stiffness in the unloading region.

The microtensile properties of plies within the bamboo were measured using micro-tensile testing. This was carried out on an Instron model 5878 electromechanical micro-testing machine (Instron, Canton, MA). Bamboo slices were first obtained along the longitudinal direction. Dog-bone shaped specimens of high, medium and low fiber density used for tensile experiment were prepared from bamboo slices with longitudinally arranged fibers (Figures 2.15 (a) and (b)). The specimens were loaded continuously at a rate of  $0.01 \text{ mm s}^{-1}$ . This was repeated three times for specimens cut from the low, medium and high fiber density regions. The resulting force–displacement data were recorded on a computer.

Four-point bending tests were performed using an Instron model 5878 (Canton, MA) servo-hydraulic testing machine. These were used to study the resistance curve behavior of the moso culm bamboo structure. The tests were conducted under displacement control, with a loading rate of  $0.01 \text{ mm s}^{-1}$ . A Celestron (Torrance, CA) digital microscope used to obtain in situ videos of crack growth and crack/material interactions. The images from this microscope were then analysed to obtain resistance curves from measurements of crack extension at known load levels. Single edge notched bend (SENB) specimens of dimensions  $4.2 \times 4.0 \times 40.0 \text{ mm}$  were used in these experiments.

The initial notch to width ratios  $a/W$  of the SENB specimens is  $\sim 0.45$  (Figure 2.16(a)). The resistance behavior of the specimens were explored along different orientations in a way that specimens notched on the outside surface orthogonal to the fiber orientation are referred to as “outside crack”, while those notched on the inside surface orthogonal to the fiber orientation are referred to as “inside crack”, while those notched on the side surface orthogonal to the fiber orientation are referred to as “side crack”.

The finite element method and an analytical approach were both used to estimate the energy release rates for SENB specimen crack geometries. A 2-D finite element modeling was carried out using ABAQUS™ software package (Simulia, Warwick, RI). The crack tip zone was distributed with collapsed elements (CPE6M) [26] to capture the stress concentrations around the crack tip. Since the four point bending specimen was symmetrical about its center line, only half of it was modeled. This helped to inhibit horizontal displacements along the center line. Vertical displacements were fixed by applying a roller support and no tractions that were applied on the crack surfaces. The experimental loads and the crack lengths obtained from the resistance-curve experiments were used in the simulation, while a 10 layer model was used to simulate the Young’s moduli that were obtained from the nanoindentation experiments. In this way, the finite element models were used to simulate the effects of the functional graded moduli on the energy release rates, which were computed from J integrals that were calculated from the path-dependent contours around the crack tip.

Figure 2.16b illustrates the set-up of a four point bend test that was used to study the fracture resistance of bi-material interfaces. The energy release rate for the interfacial crack geometries between bi-material specimen geometries is given by:

$$G = \frac{M^2(1 - \nu_2^2)}{2E_2} \left( \frac{1}{I_2} - \frac{\lambda}{I_c} \right) \quad (8)$$

where

$$M = \frac{pl}{2b} \quad (9)$$

$$\lambda = \frac{E_2(1 - \nu_1^2)}{E_1(1 - \nu_2^2)} \quad (10)$$

$$I_c = \frac{h_1^3}{12} + \lambda \frac{h_2^3}{12} + \lambda \frac{h_1 h_2 (h_1 + h_2)^2}{4(h_1 + \lambda h_2)} \quad (11)$$

$$I_2 = \frac{h_2^3}{12} \quad (12)$$

The nanoindentation results (Figure 2.17) showed that the Young's moduli decreased with increasing radial distance from the outside surface. This is consistent with the fiber density distribution presented in Figure 2.18.

The results of the microtensile tests are shown in Figures 2.19 (a) and (b). The results match the fiber density degradation observed in the bamboo specie being studied. The highest strengths correspond to the regions closest to the outside surface with the highest fiber densities, while the lowest strengths correspond to the regions farthest from the outside surfaces with the lowest fiber densities. The regions in between had intermediate strengths.

The crack/microstructure interactions observed in the resistance-curve behavior experiments are presented in Figures 2.20 (a) and (b). These show the three microstructural configurations that were examined. Cellulose fiber bridging was the major toughening mechanism in the outside and inside crack samples (Figures 2.20a), while toughening in the side sample occurred majorly due to ligament shielding (Figures 2.20b). Moreover, modest rising resistance-curve behavior was observed in all cases. Deflected crack growth that occurred along the interlaminar boundaries in the outside, inside and side specimens. In all cases, the in-situ observations of crack geometry were incorporated into finite element models that were used to compute the energy release rates. Figures 2.21 (a) and (b) present the symmetrical finite element models with deflected crack segments, where a web mesh area (Figures 2.20b) was used to capture the butterfly stress contours around the crack tip within graded elastic moduli between the layers. The energy release rates computed using the finite element simulations are presented in Figure

2.22 using hollow symbols. The energy release rates from the analytical model (Eq. (5)) are also presented in Figure 2.22, using solid symbols. The analytical and finite element results were generally in close agreement.

The implications of the results are quite significant. From establishing that the microstructural requirements for improved strengthband deformation resistance in bamboo structures are different from those required for improved toughening and resistance curve behavior, that the reduced matrix spacing in regions with high fiber densities results in lower overall toughening, while the lower fiber densities in the inside regions result in greater overall toughening to providing the potential to use bamboo as the basis for the bio-inspired design of future eco-friendly synthetic composite materials.

However, the results of this investigation suggest that there is a need for intensive research into the detailed behavior of many species of bamboos existing in abundance in tropical and subtropical parts of the world. The findings of cellulose bridging and ligament bridging may also explain the superior mechanical properties of other biological materials, such as seashells, establishing that there are challenges for the future which could contribute effectively to ecological and sustainable development.

### **2.3 State of the Art in Biomimetics**

Nathan et al [18] reviewed the current state of the art in biomimetics by providing answers to the following questions:

- a) Where is biomimetic research published?
- b) How rapidly is the subject of biomimetics expanding?
- c) What subjects does biomimetics encompass? and
- d) Are there research communities within biomimetics?

The study was restricted to biomimetics in engineering and related disciplines. It was found that most articles were published in journals - 57% of 18 000, and the rest in conference proceedings.

The leading journals and conference proceedings publishing biomimetics articles were identified as shown in Figure 2.23 and Tables 2.5 and 2.6.

His findings revealed that there has been a boom in bioinspired research between the mid '90s and this century. From barely hundred publications per annum in the mid '90s, it has grown to 3 000 per annum currently. This rather exponential growth has far surpassed what science alone has in general which is an average of 6% yearly and doubles biannually [19].

What biomimetics covers in terms of research field was evaluated by considering individual topics that make up biomimetic research. Top hundred most common topics were then arranged in order of occurrence from a data base of 18 000 publications on biomimetics as depicted in Table 2.7. The diversity of the topics found shows that variety of research topics were inspired by nature given the words like polymer, fish, collagen, muscle, vision, composite, cells, bionics, bioinspired, etc.

There are five distinct interconnected fields within biomimetics as a research area. This was established via the application of techniques from network theory to a graph of frequent biomimetic topics linked given by common pairings within the titles of papers Figure 2.23. The five identifiable research themes are therefore: robotics and control; ethology-based robotics; biomimetic actuators; biomaterials science and structural bioengineering.

## **2.4 Bioinspired Design Approaches**

Presently, there is no clear understanding of the procedure for bioinspired design as a design activity. However, two approaches have emerged in practice: (i) problem-based bioinspired design and (ii) solution-based bioinspired design [20]. Each of these approaches has its features and methodology.

### **2.4.1 Problem-Based Bioinspired Design**

According to Helms et al. [20] problem-driven BID has sequential approach though non-linear and quite iterative. The features of this method of BID are presented by Abdulkadir E. [21] as:

- It examines biological material in search of solution to an identified and defined engineering problem in mind;
- It partly imitate biological material;
- It is quite systematic, and
- It is often used in machine design.

The step-by-step approach of problem-driven BID as identified by Helms et al. [20] is:

1. Problem definition;
2. Reframe the problem;
3. Biological solution search;
4. Define the biological solution;
5. Principle extraction;
6. Principle application;

### **2.4.2 Solution-Based Bioinspired Design**

Like problem-driven BID solution-driven BID is also sequential, non-linear, and iterative [18]. Abdulkadir [21] describes its features as follows:

- It studies specific biological material objectively without bias for any particular engineering problem;
- It tends to wholly imitate the biological material;
- It is quite empirical and less systematic, and
- It is often used in search of new materials and devices.

Helms et al. [20] identified its step-by-step approach as presented below:

1. Biological solution identification
2. Define the biological solution
3. Principle extraction
4. Reframe the solution
5. Problem search
6. Problem definition
7. Principle application

## References

1. **Leonard D. A. E et. al.** Engineering Design. [ed.] Frank Kreith. *Mechanical Engineering Handbook*. s.l. : CRC Press LLC, 1999.
2. **Michael E. H., Swaroop V. and Ashok G.** *Compound Analogical Design, Or How to Make a Surfboard Disappear* . Design Intelligence Laboratory, School of Interactive Computing , Georgia Institute of Technology, Atlanta, Georgia, USA . Atlanta : s.n., 2006.
3. **C., Tomasz A. and Joanna.** Bio-inspiration: Learning Creative Design Principia. [ed.] Ian F. C. Smith. *Intelligent Computing in Engineering and Architecture*. Berlin Heidelberg : Springer Berlin Heidelberg, 2006.
4. **Meyers, M. A., Chen, P. Albert, Y. L., Yasuaki, S.** 2008. *Biological Materials: Structure and Mechanical Properties*. Progress in Materials Science. 53, pp. 1-206.
5. **NAGEL J. K. S. et. al.,** *Function-based, biologically inspired concept generation*. Cambridge : Cambridge University Press 2010 0890-0604/10 \$25.00, 2010, Artificial Intelligence for Engineering Design, Analysis and Manufacturing, Vol. 24, pp. 521-535.
6. **Brebbia, C.A., Sucharov, L.J., & Pascolo, P., [ed.]** *Proc. 1st Int. Conf., Design and Nature I: Comparing Design in Nature With Science and Engineering*. Southampton : Wessex Institute of Technology., 2002.
7. **Agrawal S. K.** [Online] 2007. <http://mechsys4.me.udel.edu/research/birdproject/>.

8. **Van der Spiegel, J. and Nishimura, M.** *Proc. IEEE Conf. Electron Devices and Solid-State Circuits: Biologically inspired vision sensor for the detection of higher-level image features.* 2003.
9. **Rhee, H., Horstemeyer, M. F., Hwang, Y., Lim, H., El Kadiri, H., Trim, W.** *A study on the structure and mechanical behavior of the Terrapene carolina carapace: A pathway to design bio-inspired synthetic composites.* s.l. : Elsevier, 2009, Materials Science and Engineering C, pp. 2333-2339.
10. **Wei Z., Chengwei W., Chenzhao Z.\*, and Zhen C.** *Microstructure and mechanical property of turtle shell.* : The Chinese Society of Theoretical and Applied Mechanics, 2012, Theoretical & Applied Mechanics Letters 2.
11. **Kantesh, B., Riken, R. P., Anup, K. K., Debrupa, L., Arvind, A.** *Multi-scale hierarchy of Chelydra serpentina: Microstructure and mechanical properties of turtle shell.* s.l. : Elsevier, 2011, Journal of the Mechanical Behavior of Biomedical Materials, Vol. 4, pp. 1440-1451.
12. **Bakshi, S.R., et al.** *The nanomechanical and nanoscratch properties of MWNT reinforced ultrahigh-molecular- weight polyethylene coatings.* Journal of Minerals, Metals, and Materials (JOM) 2007, 50–53.
13. **Oyen, M.L., and Cook, R.F.** *A practical guide for analysis of nanoindentation data.* Journal of the Mechanical Behavior of Biomedical Materials 2, (2009). 396–407.
14. **Tze, W.T.Y., et al.** Nanoindentation of wood cell walls: continuous stiffness and hardness measurements. Composites Part A 38, (2007). 945–953.
15. **Wei, G., et al.** *Nanomechanical characterization of human hair using nanoindentation and SEM.* Ultramicroscopy 105 (2005), 248–266.
16. **Zhu, W., et al.** *Nanoindentation mapping of mechanical properties of cement paste and natural rocks.* Materials Characterization 58 (2007), 1189–1198.
17. **Tan, T., Rahbar, N., Allameh, S.M., Kwofie, S., Dissmore, D., Ghavami, K., Soboyejo, W.O.** *Mechanical properties of functionally graded hierarchical bamboo structures.* Acta Biomater (2011), doi:10.1016/j.actbio.2011.06.008
18. **Nathan F. L., Paul V. and Tony J. P.** *The State of the Art in Biomimetics.*, s.l. : IOPScience, January 9, 2013, Bioinspiration & Biomimetics, Vol. 8(1).

19. **Larsen P. O. and Markus V. I.**, *The rate of growth in scientific publication and the decline in coverage provided by Science Citation Index*. 2010, *Scientometrics*, Vol. 84 (3), pp. 575-603

20. **Michael H., Swaroop S. V. and Ashok K. G.** *Biologically inspired design: process and products*. Atlanta : Elsevier Ltd., 2009, Vol. 30.

21. **Abdulkadir E.** 2010. *BioMimetic/BioInspired Robots and Mechatronics Engineering Design*. PowerPoint Presentation at Department of Mechatronics Engineering Atılım University Ankara, Turkey. Accessed 18 June 2012, 03:53 p.m.

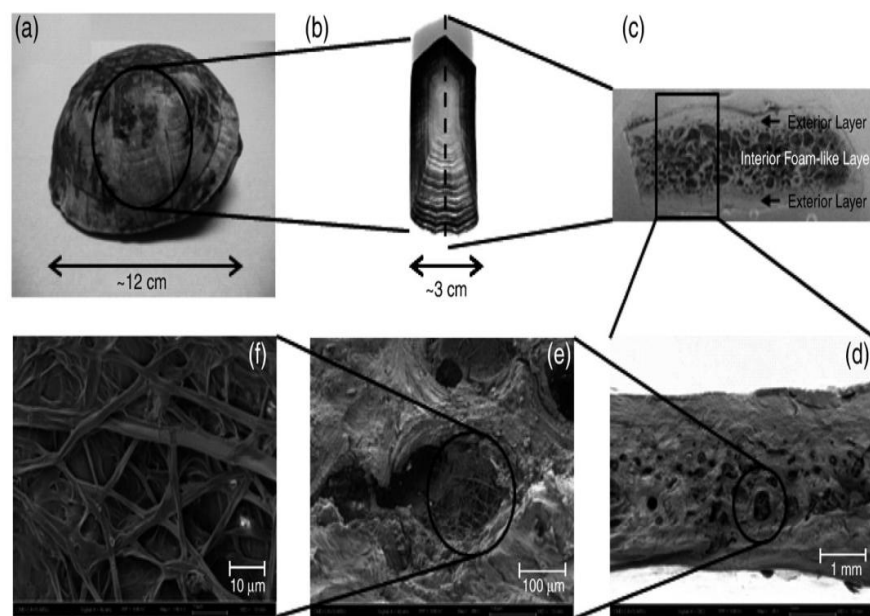


Figure 2.1: Multiscale hierarchy and structure of the turtle shell; (a) a morphology of the turtle shell carapace, (b) a costal scute showing the successive growth pattern, (c) a cross-sectional view of the carapace showing composite layers, (d) an SEM micrograph of a fracture surface, (e) an SEM micrograph of a cell structure, and (f) an SEM micrograph of a fibrous structure inside of the cell.

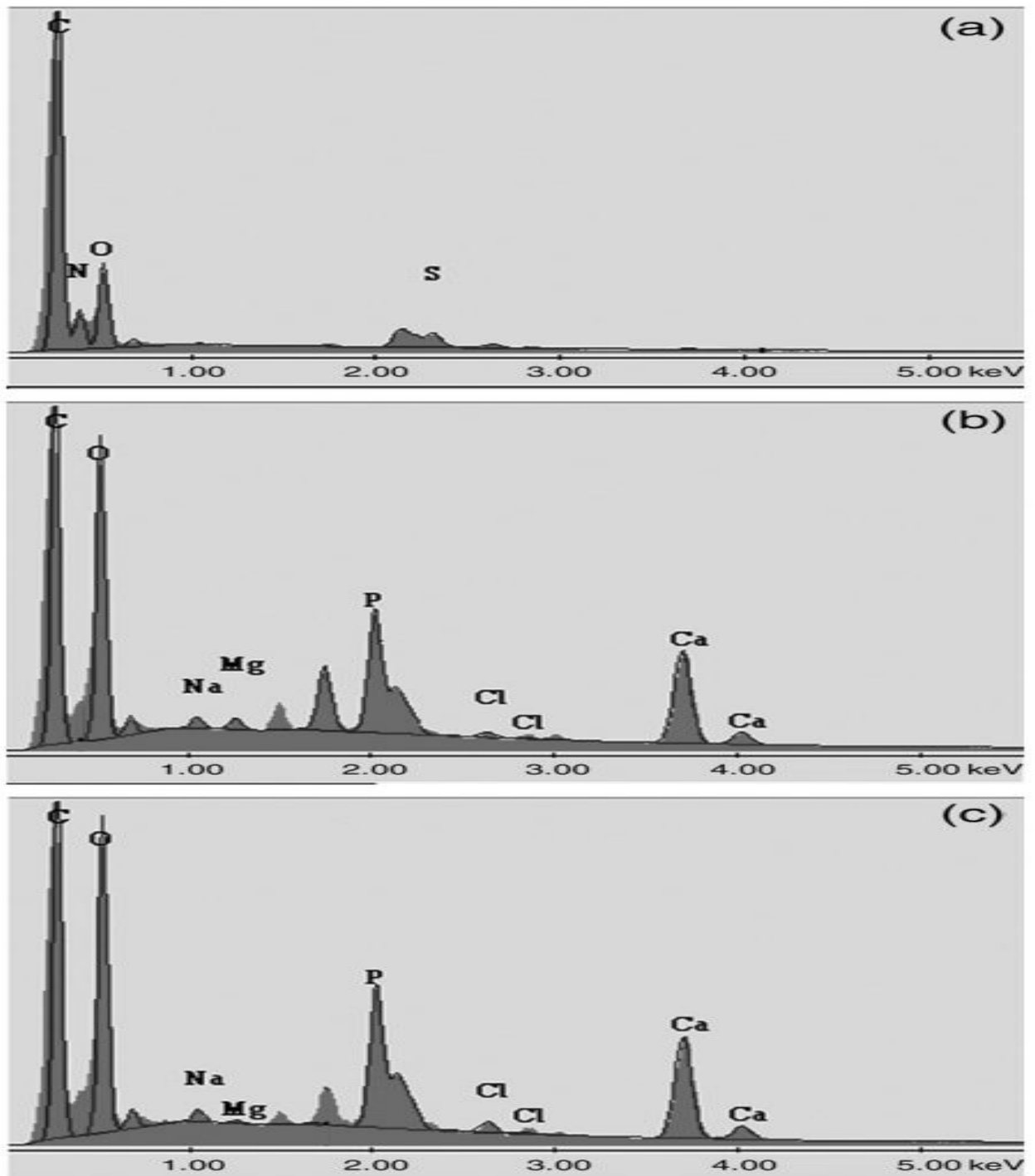


Figure 2.2: Chemical analysis results obtained from different surfaces of the turtle shell carapace: (a) the outermost keratin layer, (b) underneath the keratin layer, and (c) inside surface.

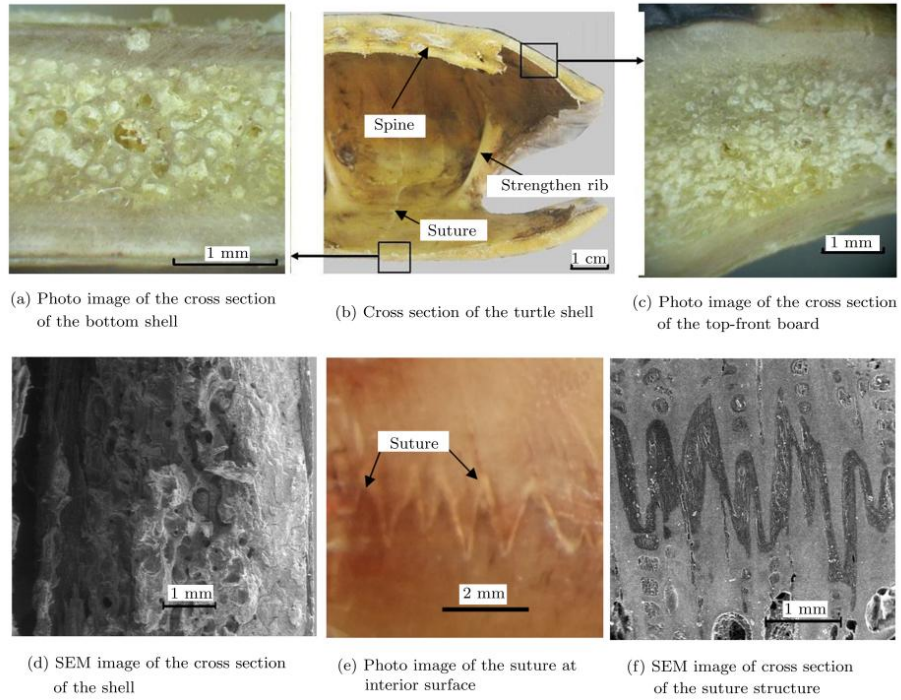


Figure 2.3: Microstructure of the turtle shell of *Trachemys scripta*.

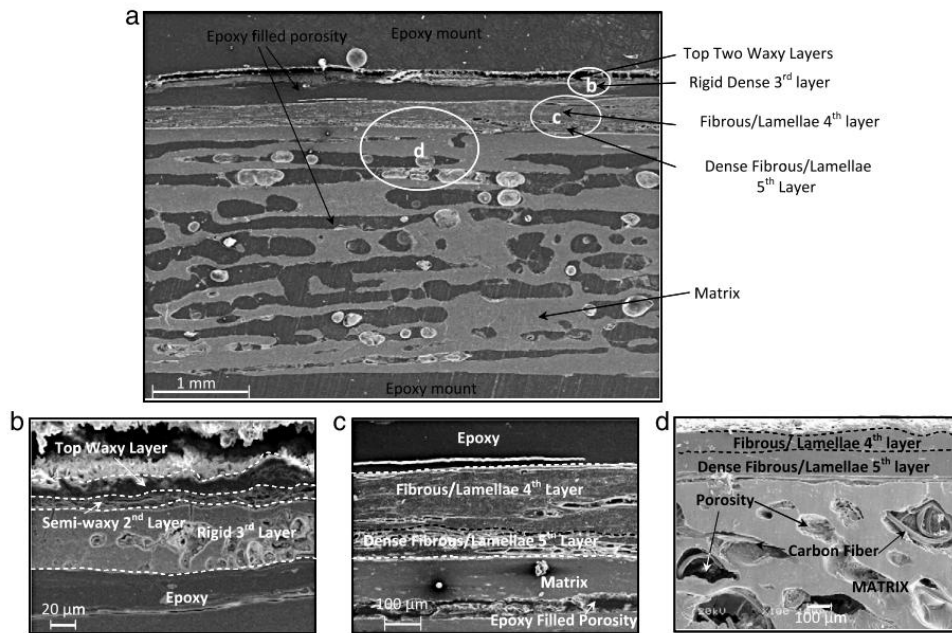


Figure 2.4: Cross-sectional of the *Chelydra serpentina*'s carapace eliciting (a) a composite sandwich structure, (b) top three layers showing the top two waxy and the rigid 3rd layer,

(c) carbonaceous lamellae 4th and 5th layers, and (d) inner structure eliciting ~ 50%–60% porous matrix (fractured and polished cross-section without epoxy infiltration).

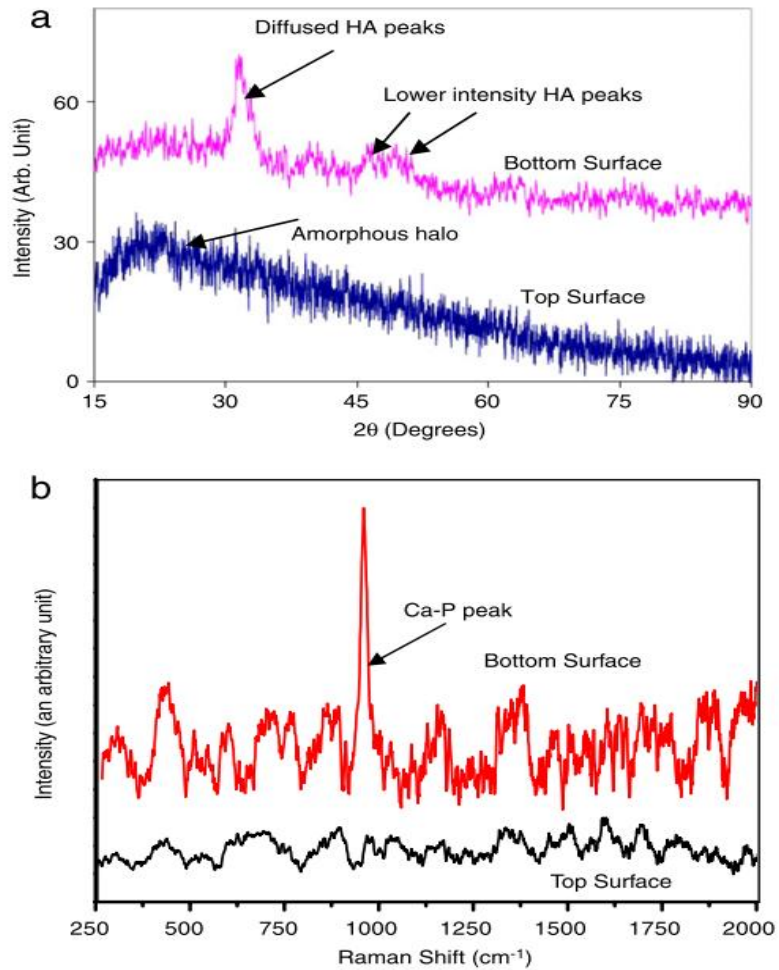


Fig. 2.5: (a) X-ray diffraction pattern eliciting diffused hydroxyapatite (HA) peak and (b) Raman spectrum showing presence of amorphous top surface and calcium-phosphate in the bottom surface of the turtle's carapace.

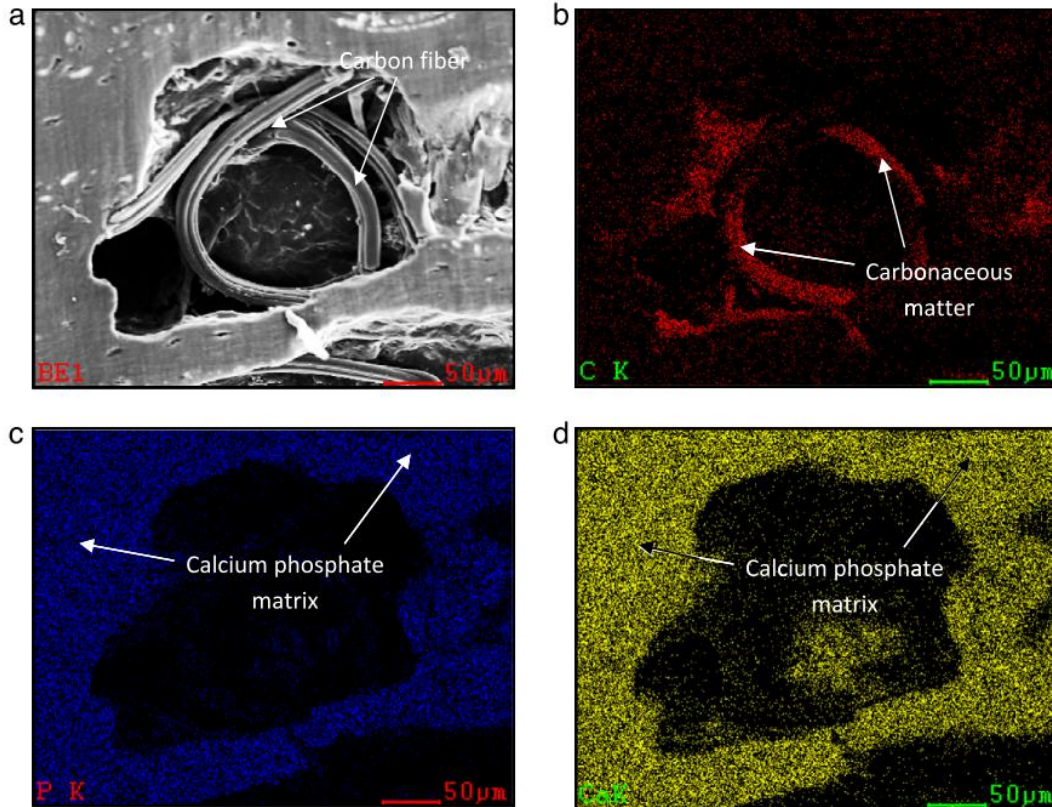


Figure 2.6: Cross-sectional SEM image of (a) Turtle's carapace, and elemental mapping of (b) carbon, (c) phosphorous, and (d) calcium eliciting the presence of carbon fibers in the calcium phosphate matrix.

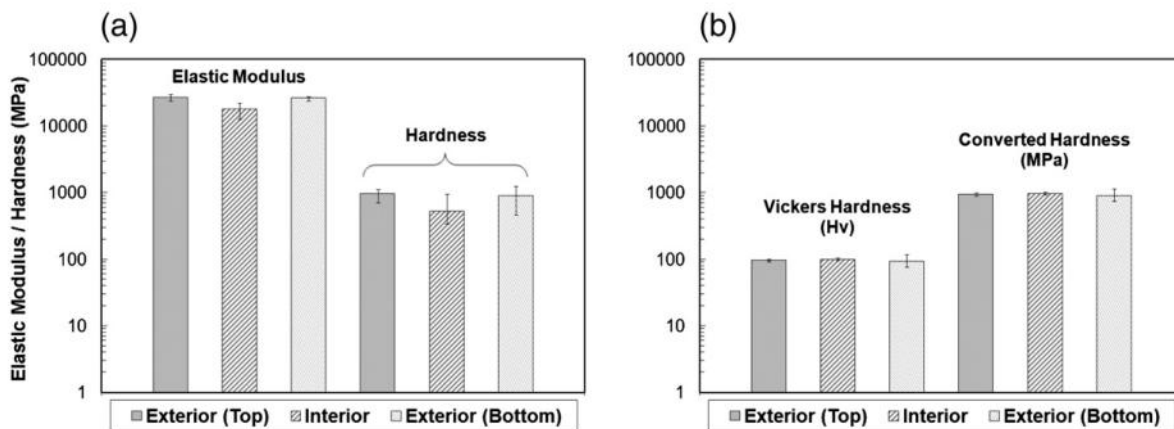


Figure 2.7: Indentation test results obtained from (a) nano-indentation and (b) Vickers hardness tests on the side surface of the turtle shell carapace.

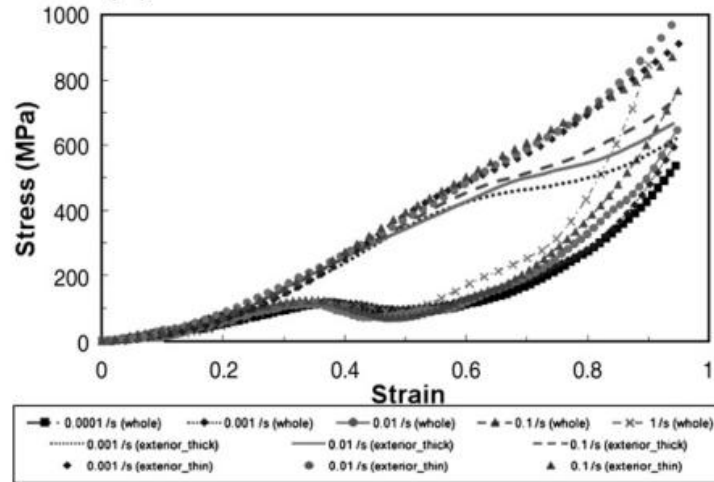


Figure 2.8: Stress/strain curves from the quasi-static compression test results on the turtle shell carapace coupon specimens under various strain rates and specimen geometries.

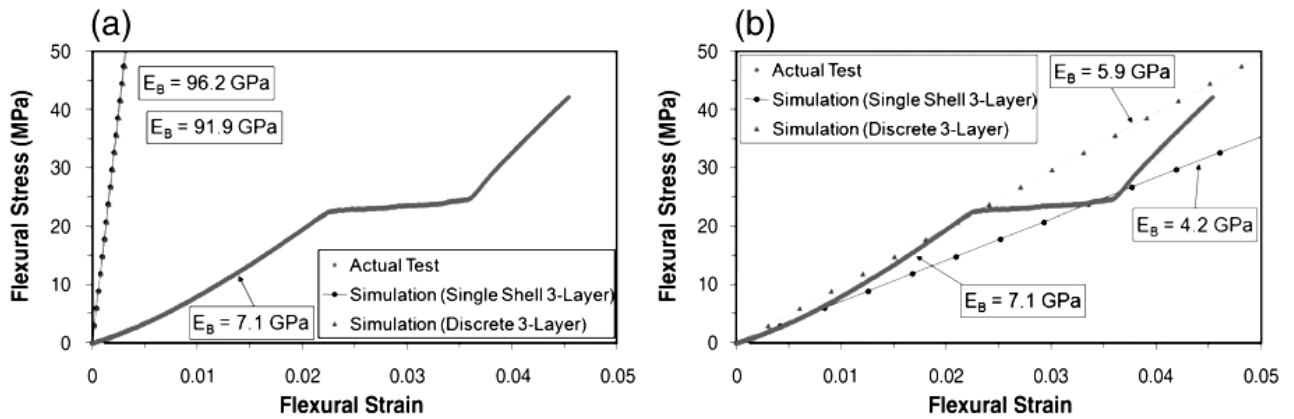


Figure 2.9: Comparison of three-point bending test results obtained from actual data and ABAQUS finite element simulations; (a) without considering foam material effect, and (b) considering foam material effect.

	Single shell three-layer	Discrete three-layer
Number of elements	2904	8712
Number of nodes	8505	19,811
Number of degrees of freedom	51,030	110,463

Table 2.1: Finite element simulation conditions.

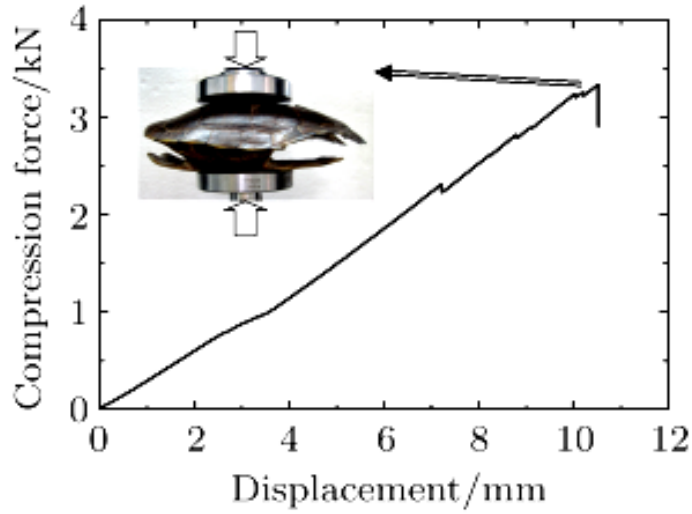


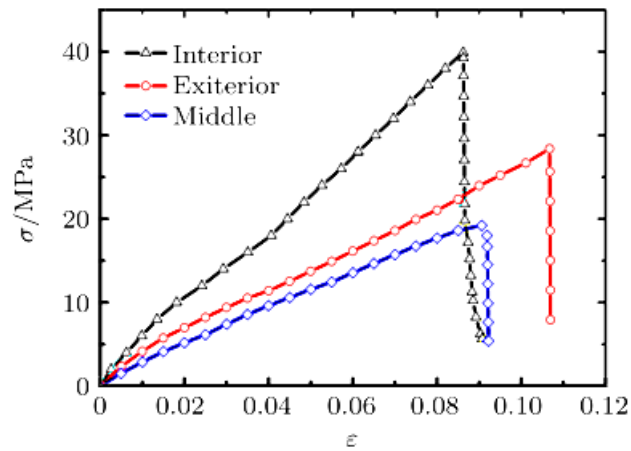
Figure 2.10: Load-displacement curve of Compression failure tests of Ts shell.

Location	Interior	Exterior	Middle
Initial modulus/MPa	985	530	315
Final modulus/MPa	500	256	230
Tensile strength/MPa	40	28	19

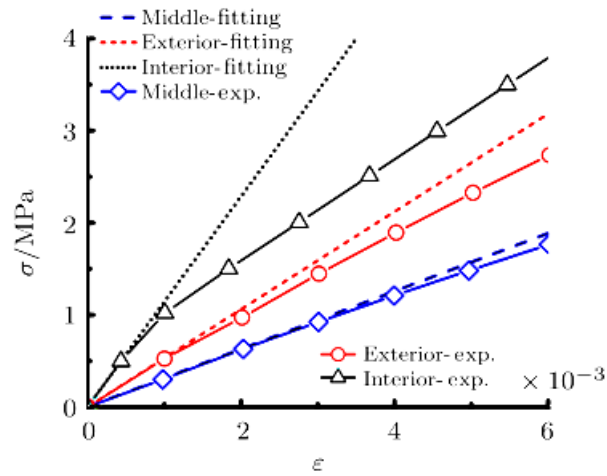
Table 2.2: The tensile modulus and strength of Ts shell materials.

Location	Interior	Middle
Initial modulus/MPa	1 190	700
Final modulus/MPa	511	382
Tensile strength/MPa	51.8	34.5

Table 2.3: The elastic modulus and ultimate strength of Ts strengthen rib.

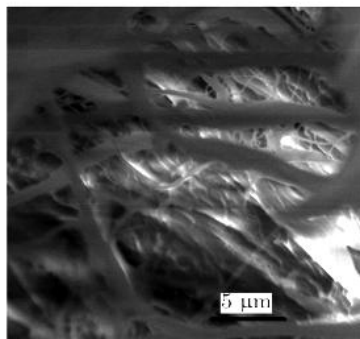


(a) The whole tensile processes

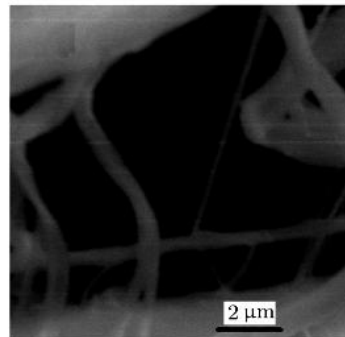


(b) The stress-strain curves at small strains

Figure 2.11: Tensile stress-strain curves at different locations of the shell.



(a)



(b)

Figure 2.12. The fiber beams enhancing the thin composite film located on the inside surface.

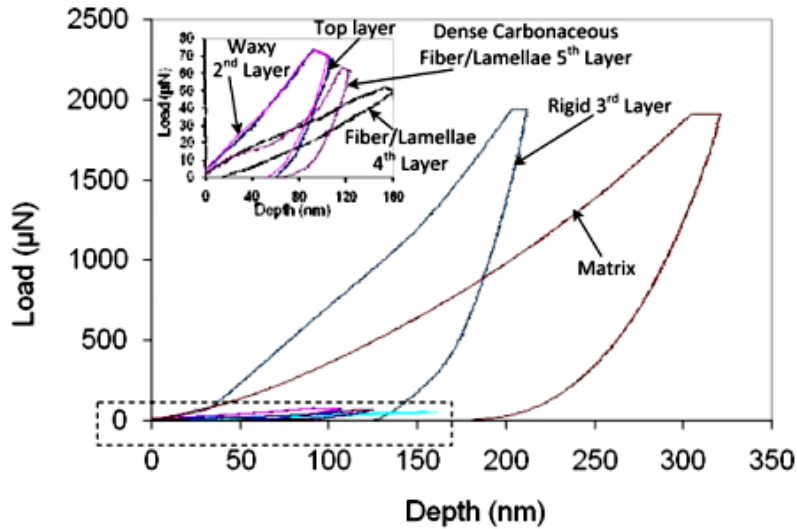


Figure 2.13: Load indentation-depth profile of the various layers, with the main image showing the structural rigid dense 3rd layer and matrix, and the inset showing a zoomed image of the dotted box for the top layer, waxy 2nd layer, and the two carbonaceous lamellae/fibrous 4th and 5th layers of the turtle’s carapace.

Layer	Thickness (µm)	Comments	$h_{\text{final}}$ (nm)	$h_{\text{res.}}$ (nm)	E (GPa)	H (MPa)	$\nu$ (Poisson's ratio)	Elasticity index
Top layer	10–15	Waxy surface	103.5	59.3	$2.03 \pm 0.18$	$74.3 \pm 20.1$	0.40	0.43
2nd layer	5–10	Semi-waxy layer	63.6	29.5	$8.25 \pm 1.71$	$208.3 \pm 32.8$	0.40	0.54
3rd layer	50	Ceramic-type dense layer	211.7	125.9	$22.15 \pm 1.99$	$522.2 \pm 75.7$	0.225	0.41
4th layer	175	Carbonaceous lamellae/fibrous structure	162.0	14.5	$0.47 \pm 0.07$	$53.7 \pm 7.7$	0.25	0.91
5th layer	75	Dense carbonaceous lamellae/fibrous structure	124.7	63.9	$1.48 \pm 0.35$	$72.0 \pm 23.3$	0.25	0.49
Matrix	3000	Matrix (~50%–60% porous). Pores have carbon fibers	320.9	182.6	$11.34 \pm 0.83$	$253.4 \pm 20.7$	0.225	0.43

$h_{\text{final}}$  is the maximum depth,  $h_{\text{res.}}$  is the residual depth of the indentation. Elasticity index is given as:  $(h_{\text{final}} - h_{\text{res.}})/h_{\text{final}}$ .

Table 2.4: Construct of the layered structure in a turtle shell with consequent mechanical properties of each layer.

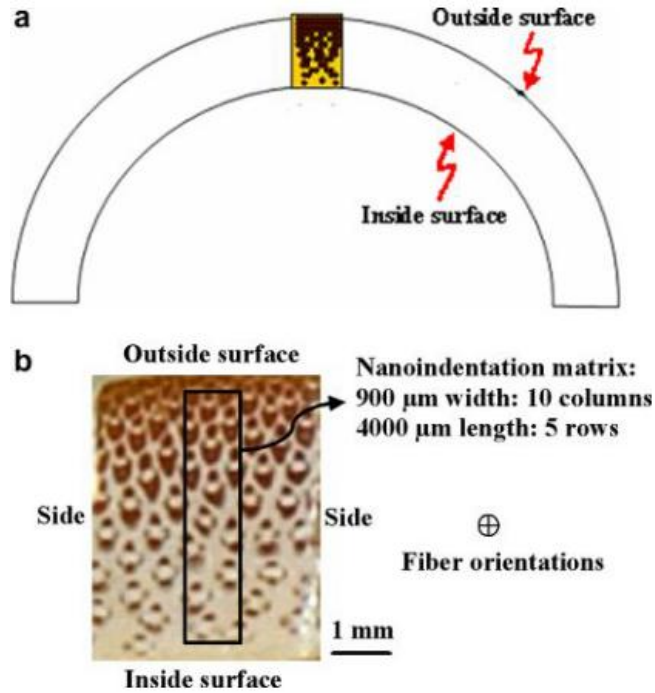


Figure 2.14: Schematics of (a) the samples prepared from bamboo and (b) cross-section of the samples and nanoindentation matrix.

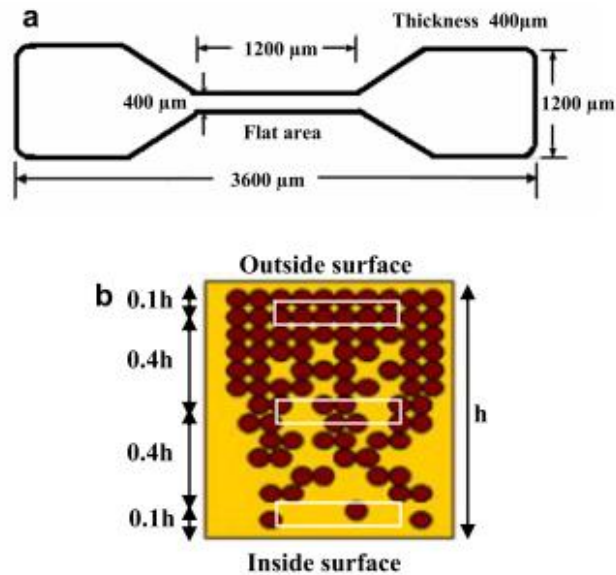


Figure 2.15: (a) A schematic of the dog bone tensile test sample. (b) A schematic of microtensile sample locations (samples are fabricated along the fiber orientations).

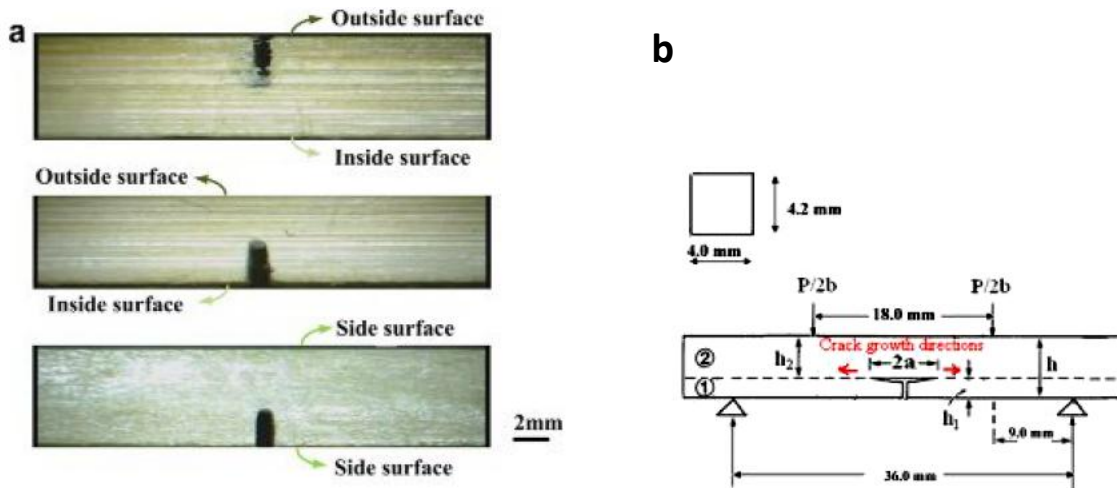


Figure 2.16: (a) Schematics of the four point bending sample from the outside, inside and side crack orientations. (b) A schematic of the experimental set-up and beam cross-section for the four point bending experiment.

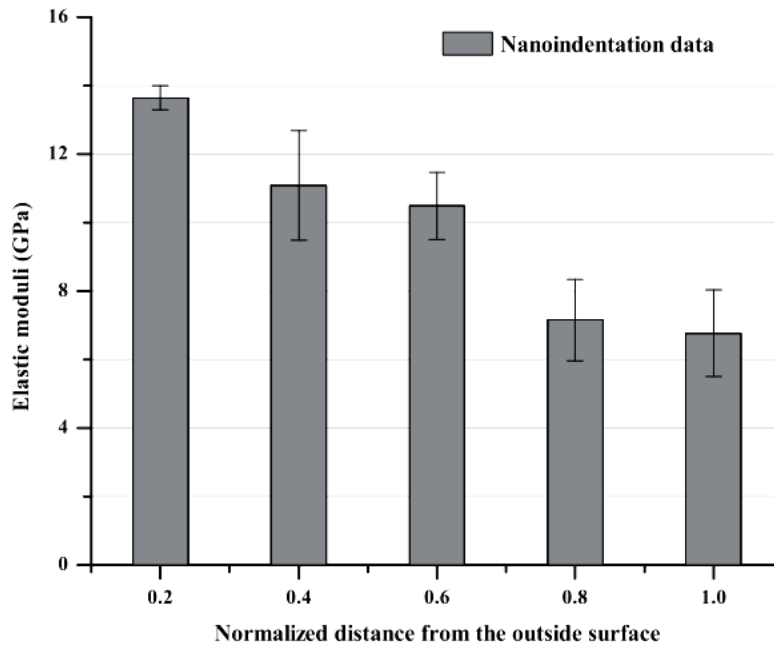


Figure 2.17: The Young's moduli distribution along the radial direction of the bamboo cross-section.

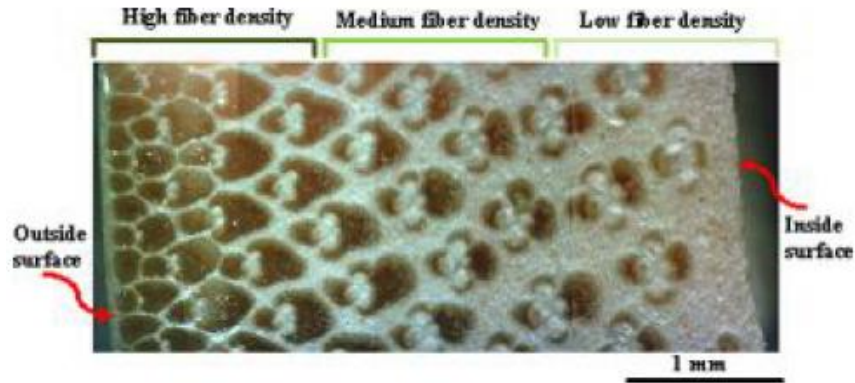


Figure 2.18: An optical image of the functionally graded mesostructure of bamboo.

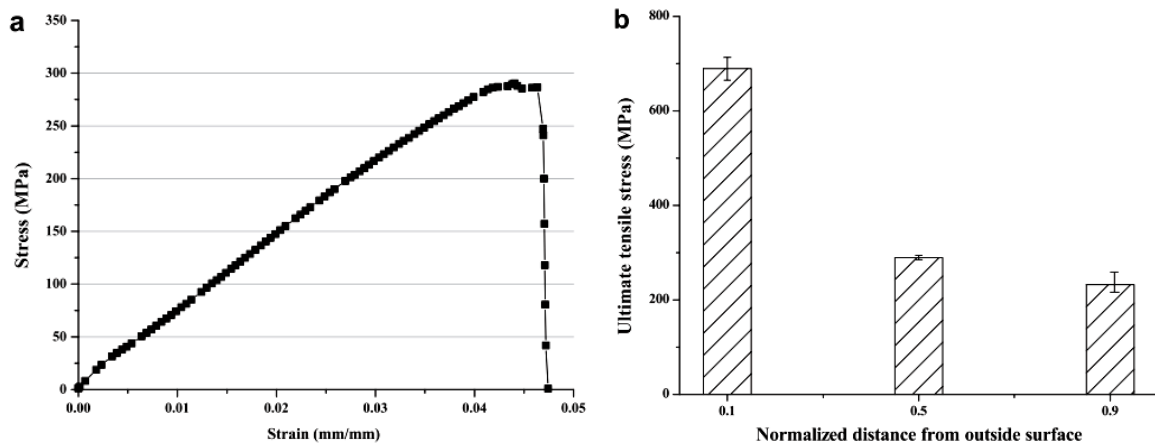


Figure 2.19: (a) A representative stress–strain curve for the bamboo microtensile experiment. (b) Tensile strength of the outside, side and inside specimens.

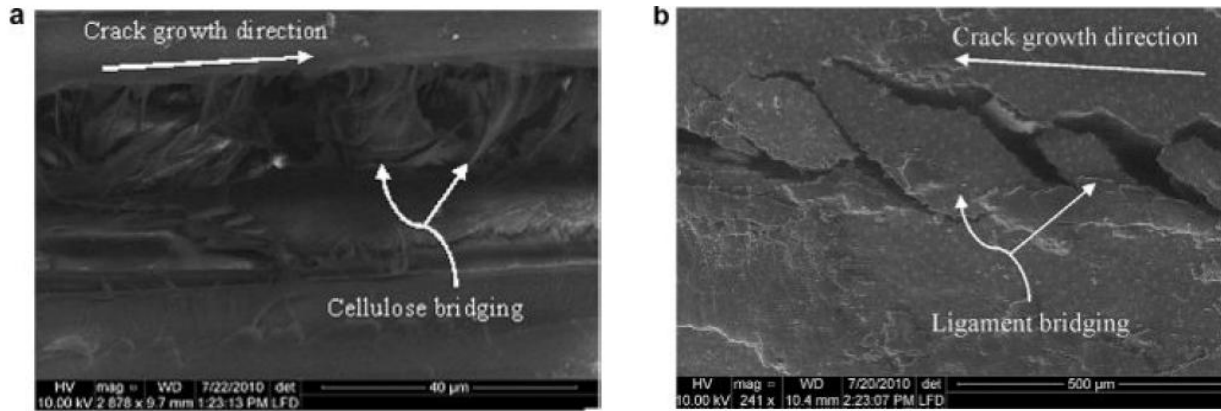


Figure 2.20: Crack growth for moso culm bamboo. (a) SEM image of cellulose bridging in the outside crack SENB sample. (b) SEM image of ligament bridging in the side crack SENB sample.

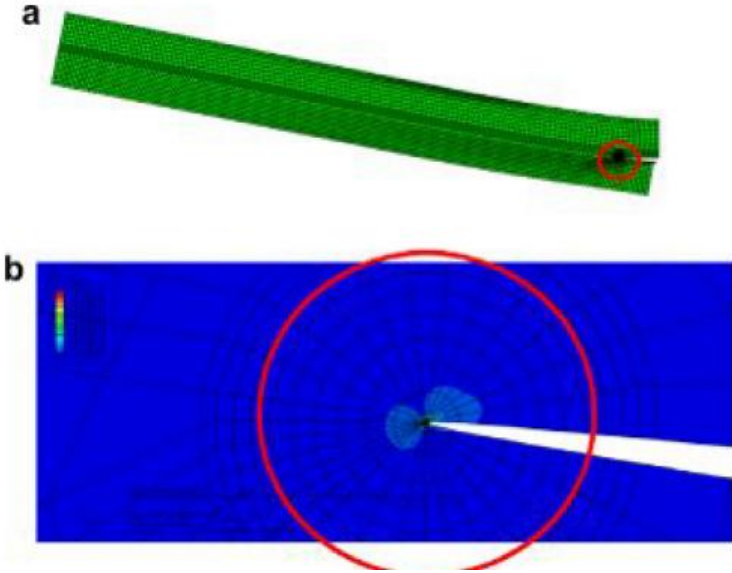


Figure 2.21: (a) An ABAQUS deformed finite element mesh for the symmetrical SENB crack model during the four point bending test. (b) The stress concentration contour around the crack tip under the registered loads and crack lengths.

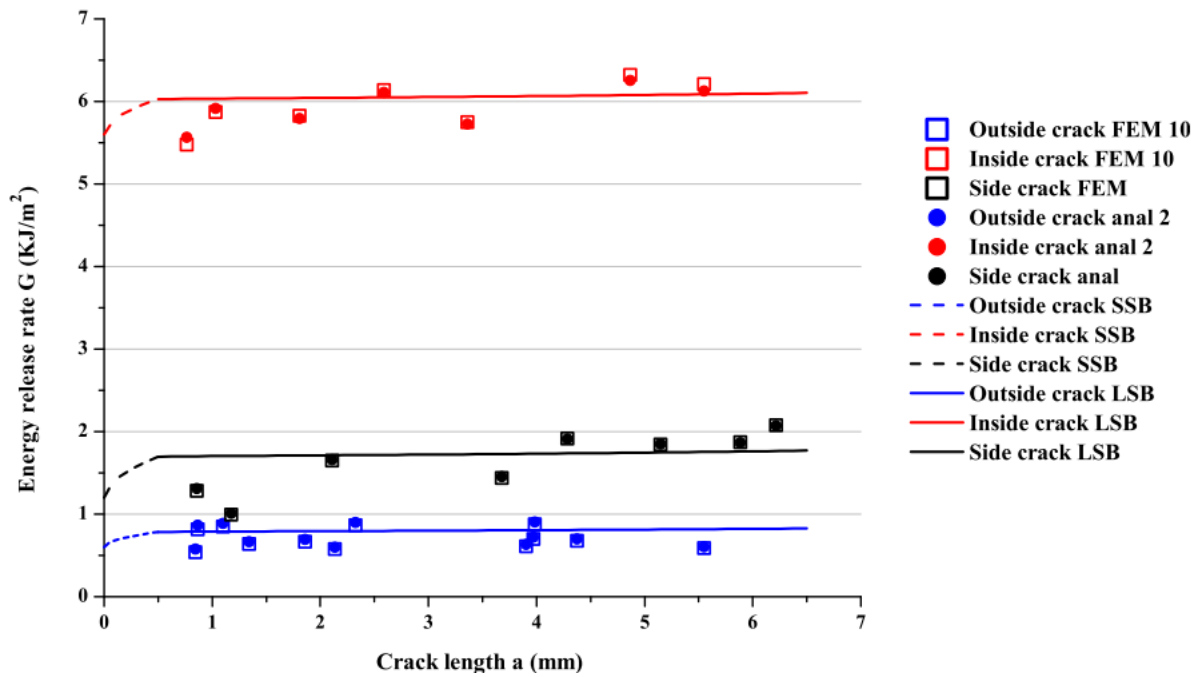


Figure 2.22: Resistance curve results for moso culm bamboo.

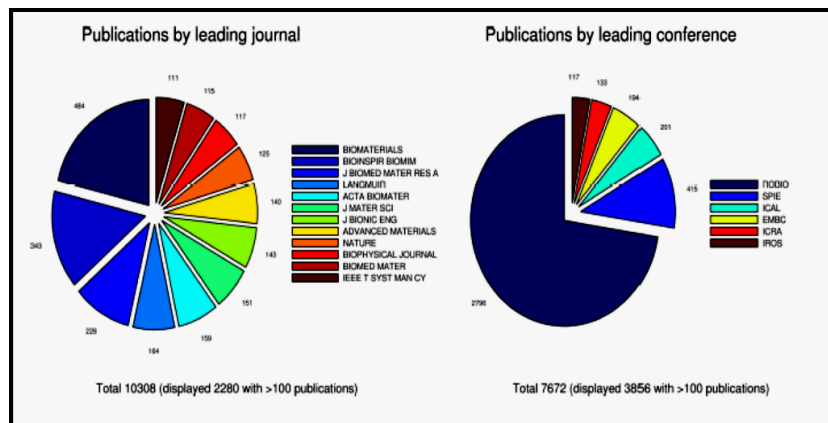


Figure 2.23: Journals and conferences publishing research on biomimetics.

Abbreviation	Journal	Publisher	Impact (2011)	Papers (2011)
BIOMATERIALS	Biomaterials	Elsevier	7.4	55/1007
BIOINSPIR BIOMIM	Bioinspiration & Biomimetics	IOP	2.0	89/89
J BIOMED MATER RES A	Journal of Biomedical Materials Research A	Wiley	2.6	18/270
LANGMUIR	Langmuir	ACS	4.1	48/1936
ACTA BIOMATER	Acta Biomaterialia	Elsevier	4.9	27/454
J MATER SCI	Journal of Materials Science: Materials in Medicine	Elsevier	2.3	18/285
J BIONIC ENG	Journal of Bionic Engineering	Elsevier	1.0	25/52
ADVANCED MATERIALS	Advanced Materials	Wiley	13.9	27/789
NATURE	Nature	NPG	36.0	20/841
BIOPHYS J	Biophysical Journal	Cell	3.7	6/696
BIOMED MATER	Biomedical Materials	IOP	2.1	27/170
IEEE T SYST MAN CY	IEEE Transactions on Systems, Man & Cybernetics	IEEE	2.1	7/109

Table 2.5: Leading journals publishing research on biomimetics.

Abbreviation	Conference	Abstracts & papers (2011)
ROBIO	Robotics & Biomimetics	536/536
SPIE	International Society for Photonics and Optics	62/2800
ICAL	International Conference on Automation & Logistics	42/107
EMBC	Engineering in Medicine & Biology Conference	23/2100
ICRA	International Conference on Robotics & Automation	19/1032
IROS	Intelligent Robots & Systems	8/719

Table 2.6: Leading conferences publishing research on biomimetics.

Word	Frequency (%)	Word	Frequency (%)	Word	Frequency (%)	Word	Frequency (%)
biomimetic	17.5	composite	2.7	fish	1.7	active	1.2
robot	13.0	development	2.7	mobile	1.6	collagen	1.2
based	11.6	bone	2.6	optimization	1.6	assembly	1.2
model	7.5	novel	2.6	effect	1.6	vision	1.2
design	6.8	materials	2.4	simulation	1.6	underwater	1.2
control	6.7	new	2.3	learning	1.5	membranes	1.1
bionic	5.7	synthesis	2.2	high	1.5	acid	1.1
inspired	4.1	method	2.2	mechanical	1.5	behavior	1.1
application	3.9	approach	2.2	characterization	1.5	peptide	1.1
human	3.8	bioinspired	2.1	formation	1.5	nano	1.1
analysis	3.5	research	2.1	detection	1.5	vitro	1.1
study	3.4	properties	2.0	fabrication	1.4	force	1.1
engineering	3.3	neural	2.0	hydroxyapatite	1.4	scaffold	1.1
sensor	3.2	like	1.9	vehicle	1.4	technology	1.1
tissue	3.2	protein	1.9	calcium	1.4	planning	1.0
structure	3.1	motion	1.9	adhesion	1.3	experimental	1.0
polymer	3.0	recognition	1.9	hybrid	1.3	environment	1.0
artificial	3.0	actuator	1.8	molecular	1.3	pattern	1.0
surface	2.9	cells	1.8	performance	1.3	effects	1.0
self	2.8	mechanism	1.8	poly	1.3	phosphate	1.0
network	2.7	surfaces	1.8	muscle	1.3	processing	1.0
algorithm	2.7	multi	1.8	apatite	1.3	visual	1.0
bio	2.7	micro	1.7	membrane	1.2	3d	1.0
cell	2.7	dynamic	1.7	time	1.2	structural	1.0
biological	2.7	scaffolds	1.7	adaptive	1.2	information	1.0

Table 2.7: Leading conferences publishing research on biomimetics.

## **3.0 Characterization of the Multi-Scale Structure of *Kinixys erosa* Shell**

### **3.1 Introduction**

Determining which features control the performance of biological materials is the first step in Biomimetics [1]. In the global world of biological materials, ‘hard’ biological materials are prominent to researchers for their unique mechanical features (e.g. stiffness, strength, and toughness) [1, 2]. Characterization is therefore, necessary to decipher the key feature underlying the multi-functionality of hard biological materials.

Common techniques that have been used to characterize biological materials (e.g. bone, shells, teeth, etc) are Microscopy, nanoindentation [3], mechanical testing, and X-ray diffraction [4]. This chapter therefore presents initial study of the structure and basic mechanical properties of the *kinixys erosa* tortoise shell. The implications of the results are then discussed as a potential source of bioinspiration for the design of shell structures that are resistant to bending.

### **3.2 The Structure of a Typical Tortoise Shell**

A tortoise shell has two parts: the upper portion-carapace and the bottom half-plastron both of which are actually made of many fused bones numbering up to 50. A bony bridge joins the carapace and the plastron along the side of the turtle.

Some turtles have a moveable joint usually in the plastron, which acts as a "hinge" and allows the turtle to pull the carapace and plastron together tightly, while the turtle retracts its body into the shell. Shells have a blood and nerve supply, so bleeding and pain can result if the shell is injured and are covered with a layer of keratin (as in fingernails or horses' hooves). The keratin is arranged in patches called scutes or shields numbering 38 on the carapace and 12 to 14 on the plastron. Figures 3.1 and 3.2 illustrate these descriptions.

The names and numbers of the scutes roughly correspond to the adjacent bones and body portions. The scutes, however, do not precisely overlap the bones. Instead, they are staggered, which helps give the shell more rigidity [5].

### **3.3 Bone Structure**

The bone structure can be divided into two distinct types of osseous (bony) tissues: cortical region and trabecular or cancellous type [6]. The cortical region is dense and comprises the outer structure or cortex of the bone, while the interior consists of the trabecular tissue, made of thin plates or trabeculae loosely meshed and porous. The pores in these trabecular regions are filled with bone marrow. The ratio of cortical to trabecular in any bone structure affects the mechanical properties of the bone.

### **3.4 Experimental Methods**

#### **3.4.1 Microstructural and compositional characterization of *Kinixys erosa* (Ke) carapace materials**

The structure of the shell bone was examined using LCD Deluxe Digital Microscope model 44345 (Celestron, Torrance). A cut section of Ke carapace bone was fine polished with emery paper and studied at a magnification of 100X. Powder X-ray diffraction (XRD) analysis of both the scute and the carapace bone of Ke were carried out using an X'Pert PRO MPD diffractometer (PANanalytical, Almelo). The XRD analysis was carried out using  $\text{CuK}\alpha$  radiation from a rotating anode generator operated at 40kV and 30mA in the range of  $2\theta = 5.0334^\circ - 79.9394^\circ$ . The shell bone was pulverized using mortar and pestle while the scute ground after cooling with liquid nitrogen. The scanning step was 0.067 degrees while the scan step times were 6.985 sec. and 59.69 sec., for the scute and the shell bone, respectively.

### **3.4.2 Micromechanical and nanomechanical characterization of *Kinixys erosa* carapace materials**

The micromechanical characterizations involved compression testing and bend testing. These were carried out on the carapace bone of Ke tortoise shell using a TIRA test-2810 Universal testing machine (TIRA GmbH, Schalkau) that was operated at a cross head speed of 0.5mm/min. The compression test samples were prepared from the marginal bones, while the bend test samples were prepared from the other parts of the shell bone. The compression test samples were cubical, while the bend test samples were rectangular blocks. Figures 3.9 - 3.12 shows the test sample geometries.

The nanomechanical characterization involved modulus and hardness measurements. These were carried out on the cortical section of the multilayered carapace bone of Ke tortoise shell using a Berkovich diamond indenter tip on a Hysitron TriboIndenter® (Hysitron, Minneapolis, MN ). The indenter tip used was a three-sided pyramidal type with an included angle of 142.3° and a tip radius of ~ 150 nm. This was used to apply a maximum loads of 5000  $\mu\text{N}$  (ramp of 200  $\mu\text{N/s}$ ).

## **3.5 Results and Discussion**

### **3.5.1 Microstructural and compositional characterization of *Kinixys erosa* (Ke) carapace materials**

The powder diffraction analysis (Figure 3.5) of the shell showed that it contains hydroxyapatite as the primary phase in the bone structure. In contrast, it suggests the scute (Figure 3.6) contains 9-Aminide nylon 6 oligomer crystals and 17-Amide nylon 6 oligomer crystal. The micro images of the cut section of the shell's bone structure obtained from the microscope revealed that it is like a sandwich composite panel. The cancellous bone structure is sandwiched in between cortical sections. Figure 3 shows the optical microscopy while Figure 3.4 presents a schematic of the layered structure. The marginal bone consists of ~ 54.5% volume fraction of trabeculae bone

sandwiched between ~ 10.9% and ~ 34.6% cortical bone sections. Also, the vertebrals and pleurals on the other hand have ~ 60% volume fraction of trabeculae bone sandwiched between ~ 20% volume fraction of cortical bone sections.

### 3.52 Micromechanical and nanomechanical characterization of *Kinixys erosa* carapace materials

The flexural strength, flexural strain, Young's modulus in bending [7], maximum ultimate bending strain [8] and stiffness of Ke bone was estimated based on the data obtained from the bending test (Table 3.1 and Figure 3.8) described in section 3.4.2 above. The estimates were done using the data into the following equations:

$$\sigma_f = \frac{Mc}{I} \quad (1)$$

$$\epsilon_f = \frac{6Dd}{L^2} \quad (2)$$

$$E_B = \frac{KL^3}{4bd^3} \quad (3)$$

$$\epsilon = \frac{Md}{2E_B I} \quad (4)$$

$$F = Kx \quad (5)$$

Where  $\sigma_f$  is the flexural strength (MPa),  $M$  is the bending moment (Nm),  $c$  is the centroid (m),  $I$  is the second moment of area ( $m^4$ ),  $F$  is the load (N),  $K$  is the stiffness (N/m),  $x$  is the deformation (m),  $D$  is the maximum deflection of the specimen center (m),  $d$  is the specimen thickness (m),  $b$  is the width of specimen (m),  $E_B$  is the Young's modulus in bending (GPa),  $\epsilon$  is the maximum ultimate bending strain.

Similarly, the compression strength was estimated based on the data obtained from the compression test (Figure 3.7) described in section 2.3 above. The estimate was done using:



### **3.53 Discussion**

The mechanical test results obtained correlate with the constituents of the *kinixys erosa* tortoise shell bone as well as its microstructure. The proportion of cancellous to cortical bone in the samples (section 3.51) tested explains the wide disparity seen in the flexural and compressive strength of *kinixys erosa* tortoise shell bone.

The compression test results presented in Figure 7 can be explained by idealizing the specimens as synthetic foams and/or honeycombs structures, since fundamental structures of the test specimens are similar to those of such cellular solids. At small strains, the specimens were deformed in a linear elastic manner due to the cell wall bending [9]. Soon after the initial linear elastic deformation, a plateau of deformation was reached, because of the buckling of the cell walls. After such a plateau of deformation, another period of linear deformation was proceeded since a densification occurred resulting in a rapid increase of compressive stress.

In addition, the behavior of the stress-strain curve shown in Figure 3.7 shows two distinct regions. The first region is such that strain increases as stress increases and tends to plateau around stress value of  $\sim 20$  MPa. It then descended to about  $\sim 12$  MPa to complete the first region (point X, Figure 3.7), marking also the beginning of the second stage. The first stage depicts the loading of the cancellous section, while the second stage shows the loading of the cortical section.

### **3.6 Summary**

A characterization of the multi-scale structure of *Kinixys erosa* carapace material is presented in this chapter. Its unique features were investigated linking structure to properties. The carapace is a sandwich composite structure with a denser exterior lamellar bone layers (cortical bone) and an interior bony network of closed-cell fibrous foam layer (cancellous bone).

The bone structure was found to contain hydroxyapatite. Flexural strength of the bone structure was found to be  $\sim 162.53 \pm 3.9 \text{ MPa}$  as against its compressive strength which was  $\sim 35.7 \pm 1.7 \text{ MPa}$ , while the stiffness was  $-22.4 \text{ KN/m}$ . The Young's modulus in bending ( $E_B$ ) is  $6.4 \text{ GPa}$  and that of the cortical layer is  $14.73 \pm 1.32 \text{ GPa}$ , with the flexural strain and maximum ultimate bending strain being  $0.35$  and  $0.025$  respectively. The scute constituent could contain 9/17-Amide nylon 6 oligomer. It was also found to be resistant to concentrated acid and base; however this requires further investigation. The estimated Young's modulus ( $E_s$ ) of the cortical layer of carapace bone is  $14.73 \pm 1.32 \text{ GPa}$ .

The understanding obtained from this study could be quite significant for the design of shell structures that are resistant to bending. Also bio-mimicking the naturally engineered composition of the sandwiched structure can sustain impact and allow redistribution of the stress uniformly throughout the structural phases as occurs naturally in a turtle's carapace [10]. However, the structure may be susceptible to failure by localized compression, especially in scenarios in which the loads are perpendicular to the layers. Further work is clearly needed to study the failure modes and potential implication for bioinspired design.

## References

1. **Barthelat, F.** 2007. *Biomimetics for Next Generation Materials*. Phil. Trans. R. Soc. A 365, 2907–2919 (doi:10.1098/rsta.2007.0006).
2. **Currey, J. D.** *The design of mineralised hard tissues for their mechanical functions*. J. Exp. Biol. 202, 1999, 3285–3294.
3. **Meyers, M. A., Chen, P. Albert, Y. L., Yasuaki, S.** 2008. *Biological Materials: Structure and Mechanical Properties*. Progress in Materials Science. 53, pp. 1-206.
4. **Fengxiang Z., Anning W., Zhihua L., Shengwen H., Lijun S.** *Preparation and Characterisation of Collagen from Freshwater Fish Scales*. s.l. : Scientific Research, 2011, Food and Nutrition Sciences, Vol. 2, pp. 818-823.
5. **Foster & Smith Inc.** *Shells: Anatomy and Diseases of Turtle and Tortoise Shells*. Accessed 20 June 2012, 09:52 p.m.

6. **William F. S. and Javad H.** *Foundations of Materials Science and Engineering* 4th edition. McGraw-Hill, New York, 2006.
7. **Rhee, H., Horstemeyer, M. F., Hwang, Y., Lim, H., El Kadiri, H., Trim, W.** *A study on the structure and mechanical behavior of the Terrapene carolina carapace: A pathway to design bio-inspired synthetic composites.* s.l. : Elsevier, 2009, Materials Science and Engineering C, pp. 2333-2339.
8. **Magwene, P. M., Socha, J. J.** *Biomechanics of turtle shells: How whole shells fail in compression.* 2012. J. Exp. Zool. 9999A:1 – 13.
9. **Gibson, L. J. and Ashby, M. F.** *Cellular Solids: Structure and Properties, 2nd ed.* (Cambridge University Press, Cambridge, U.K., 1997).
10. **Kantesh, B., Riken, R. P., Anup, K. K., Debrupa, L., Arvind, A.** *Multi-scale hierarchy of Chelydra serpentina: Microstructure and mechanical properties of turtle shell.* s.l. : Elsevier, 2011, Journal of the Mechanical Behavior of Biomedical Materials, Vol. 4, pp. 1440-1451.



Figure 3.1: Carapace [C] and Plastron [P] of kinixys erosa

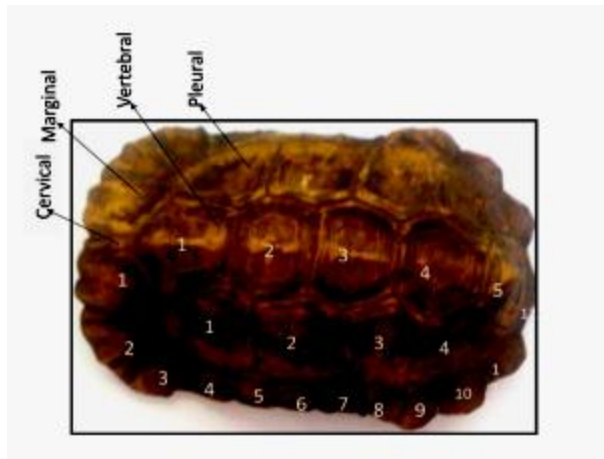


Figure 3.2: Scutes on the carapace of kinixys erosa tortoise shell

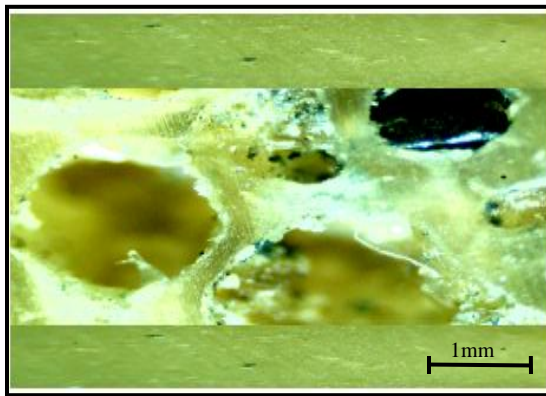


Figure 3.3: Cross section of kinixys erosa bone structure.

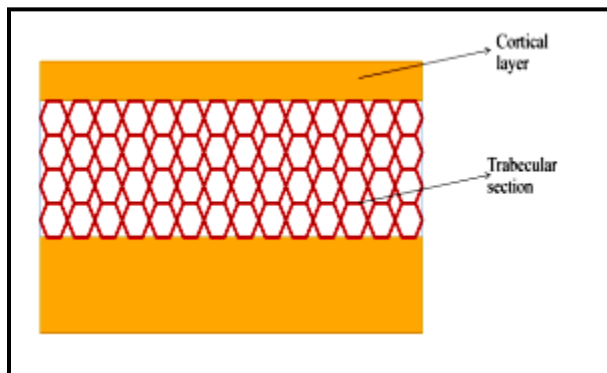


Figure 3.4: Schematic of kinixys erosa bone structure

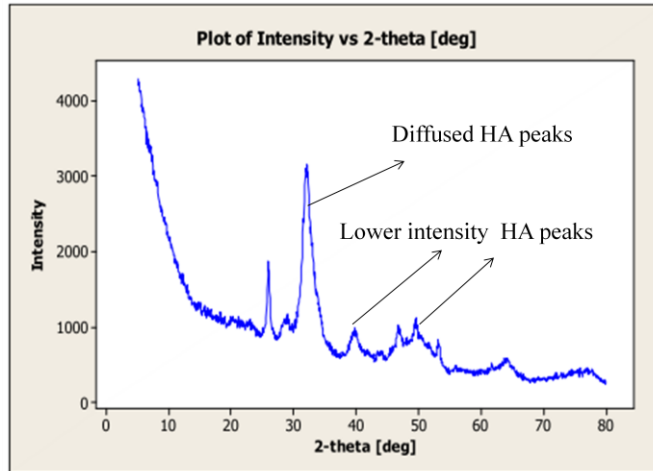


Figure 3.5: X-ray spectrum of kinixys erosa shell bone

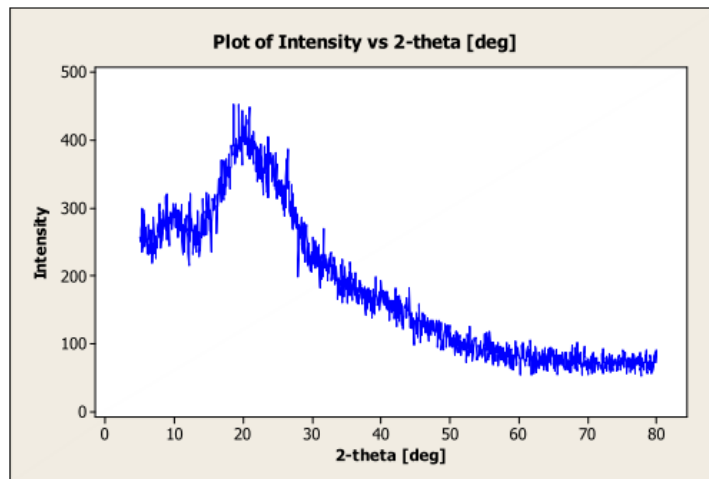


Figure 3.6: X-ray spectrum of kinixys erosa scute

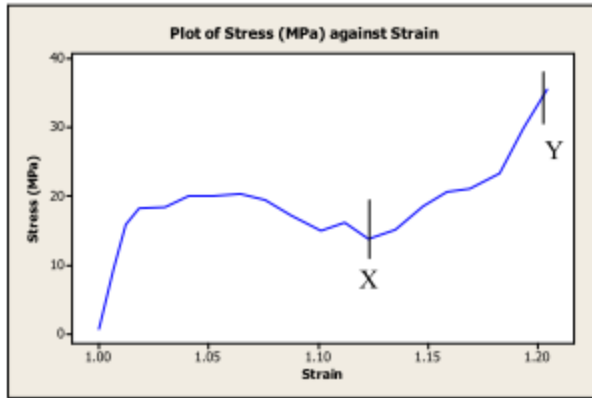


Figure 3.7: Stress-strain plot of compression test on kinixys erosa carapace bone structure

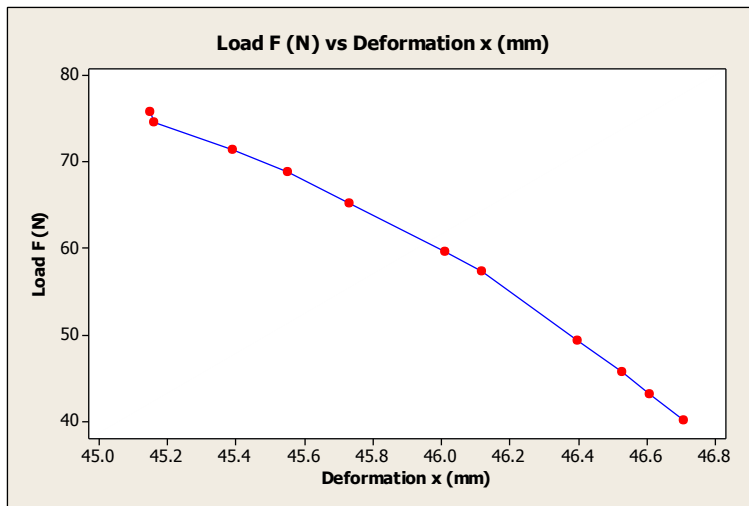


Figure 3.8: Load/deformation plot three point flexural test on kinixys erosa carapace bone structure



Figure 3.9: Compression test samples



Figure 3.10: Bend test samples

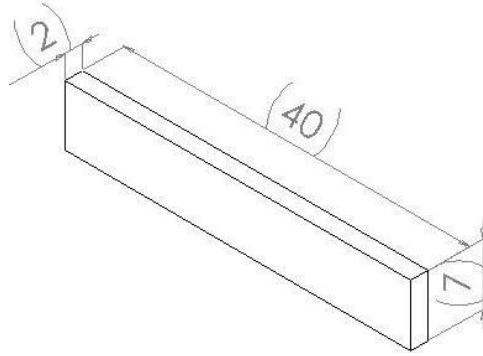


Figure 3.11: Schematic of bend test sample (all units in mm)

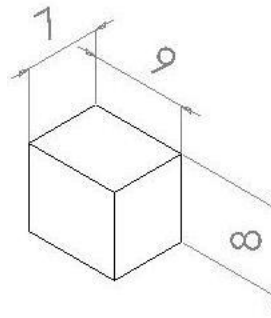


Figure 3.12: Schematic of compression test sample (all units in mm)

Load F (N)	Deformation $x$ (mm)
40.07	46.71
43.03	46.61
45.68	46.53
49.37	46.40
57.30	46.12
59.65	46.01
65.23	45.73
68.82	45.55
71.50	45.39
74.62	45.16
75.90	45.15

Table 3.1: Load-displacement data of flexural test on kinixys erosa bone structure

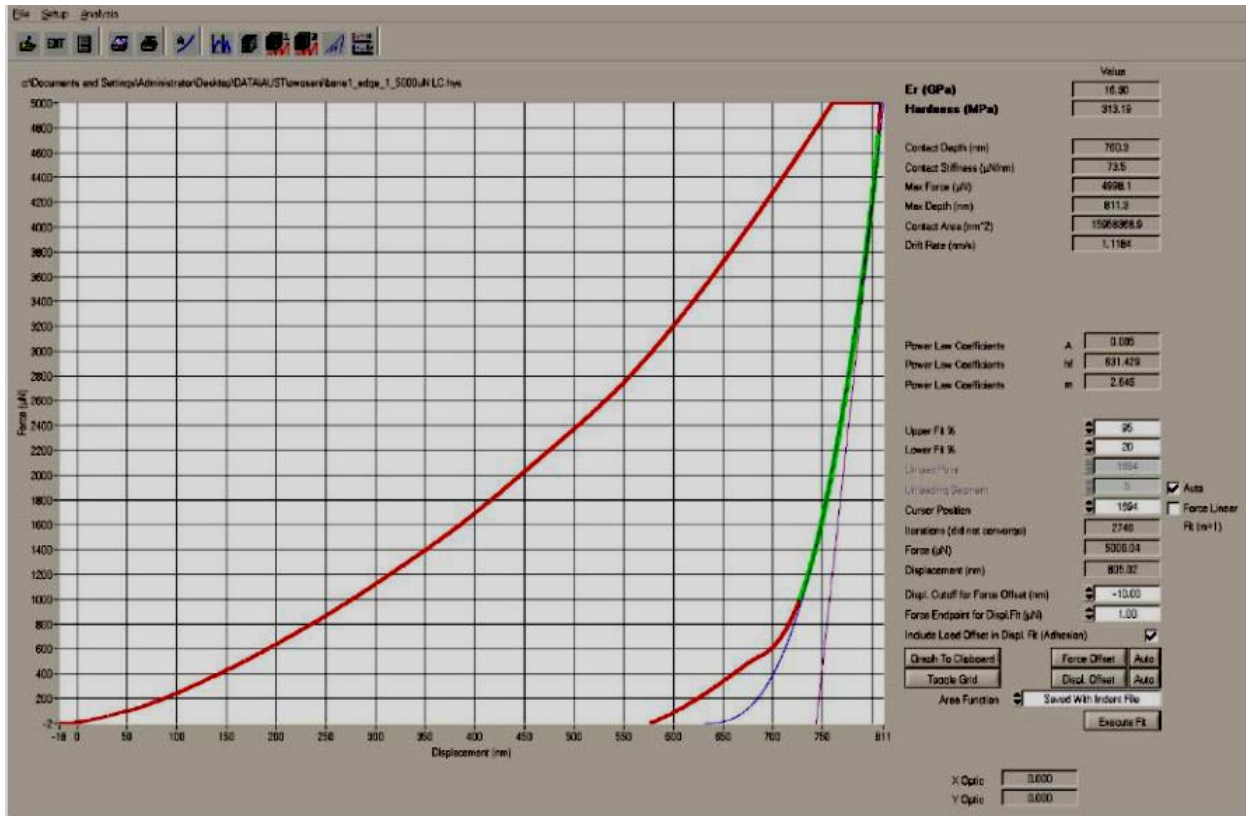


Figure 3.13: Load indentation-depth profile of the cortical layer of the multilayered carapace bone of Ke tortoise shell

## 4.0 Analytical and Computational Model of Shell Structures

### 4.1 Introduction

Shells are much more rigid structures than plates under the same external loading conditions [1]. A shell is able to transmit loads by ‘membrane’ stresses. These act parallel to the tangential plane at a given point of the middle surface and are distributed uniformly over the shell’s thickness. In contrast, the static equilibrium of a plate under the action of an external load is achieved via bending and twisting, usually accompanied by shearing forces.

This chapter presents the results of analytical and computational modelling on shell structures. Shell behaviour studied under the action of external loads. First, an analytical model is presented from shell theory [1]. The analytical predictions are then compared with predictions from a computational finite element model that was implemented using the commercial ABAQUS code (ABAQUS/CAE 6.9 Student Edition, Simulia, Warwick, RI, USA). The implications of the results are then discussed for the bioinspired design of multi-layered shell structures, as seen in *Kinixys erosa* (Ke) presented in chapter three.

### 4.2 Analytical Model Based on Theory of Shell

The analytical solution of the stress distribution, the corresponding strain and deflection of the shell under the action of a pressure load is presented, based on theory of shell. The tortoise shell was idealised as an isotropic and symmetric ellipsoidal shell of uniform thickness. See Appendix A for the full solution.

$$N_{\varphi} = \frac{-pr_2}{2} \text{ and } N_{\theta} = pr_2 \left( \frac{r_2}{2r_1} - 1 \right) \dots \dots \dots (1)$$

$$\epsilon_{\varphi} = \frac{1}{Eh} (N_{\varphi} - \nu N_{\theta}) \text{ and } \epsilon_{\theta} = \frac{1}{Eh} (N_{\theta} - \nu N_{\varphi}) \dots \dots \dots (2)$$

$$v(\varphi) = y \ln \left( \tan \frac{\varphi}{2} \right) \sin \varphi \dots \dots \dots (3)$$

$$w = y \ln \left( \tan \frac{\varphi}{2} \right) \cos \varphi - \frac{pr_2^2}{Eh} \left[ \left( \frac{r_2}{2r_1} - 1 \right) + \frac{v}{2} \right] \dots \dots \dots (4)$$

$$y = \frac{pr_1r_2}{Eh} \left[ v \left( 1 - \frac{r_2}{2r_1} \right) - \frac{1}{2} \right] - \frac{pr_2^2}{Eh} \left[ \left( \frac{r_2}{2r_1} - 1 \right) + \frac{v}{2} \right] \dots \dots \dots (5)$$

$$r_0 = r_2 \sin \varphi \dots \dots \dots (6)$$

$$r_1 = \frac{a^2 b^2}{(a^2 \sin^2 \varphi + b^2 \cos^2 \varphi)^{\frac{3}{2}}} \dots \dots \dots (7)$$

$$r_2 = \frac{a^2}{(a^2 \sin^2 \varphi + b^2 \cos^2 \varphi)^{\frac{1}{2}}} \dots \dots \dots (8)$$

$p = 1 \text{ MPa}, a = 57.5 \text{ mm}, b = 65 \text{ mm}, E = 6.4 \text{ GPa}, h = 2 \text{ mm}, v = 0.33$   
 $\varphi = 0^\circ - 90^\circ$  at a step of  $10^\circ$

Reference to the ventral/dorsal view of Ke tortoise shell **a** and **b** which are 57.5 mm and 65 mm respectively, represent the minor radius and the ellipsoidal dome height. **r<sub>0</sub>** is the radius of the cross-section of the parallel circle described by the applied pressure load **p**, which has a magnitude of 1 MPa, a form of broad load. **r<sub>1</sub>** and **r<sub>2</sub>** are the principal radii of curvature. **φ** is the distribution angle as the stress, strain, and deflection varies from O to the equator AA ( $0^\circ - 90^\circ$  at a step of  $10^\circ$ ). For a shell problem the stress is often taken as force per length, in this case, **N<sub>φ</sub>** and **N<sub>θ</sub>**. **ε<sub>φ</sub>** and **ε<sub>θ</sub>** are the radial and tangential strains respectively, while v and w are also the radial and tangential displacements respectively. The thickness h of the shell is 2 mm, while the imposed Modulus E is 6.4 GPa. The equations were analysed using MATLAB R2009b (MathWorks Inc., Natick, Massachusetts, USA).

### 4.3 Computational Finite Element Model

The finite element analyses (FEA) of the shell structure were performed using a commercial code, ABAQUS. The material properties ( $E_B = 6.4 \text{ GPa}$  and  $v = 0.33$ ) that were used in the FEA were obtained from the bending tests presented earlier in Chapter 3. A 2-D model with element

type CPS4R was established. The detailed simulation conditions are as presented in Table 4.2 below. The applied pressure load (Figure 4.8) is the same with that used in the analytical model (Section 4.2).

3-D models with element S4R were established to further demonstrate the effect of geometry cum single layer versus multilayer in shell architectures (dome). The detailed simulation conditions are presented in Table 4.3. The applied pressure load (Figure 4.11) is the same with that used in the analytical model (Section 4.2).

## **4.4 Results and Discussion**

### **4.41 Analytical Model Based on Theory of Shell**

The data obtained from the analytical model are presented in Table 4.1. The typical stress contour plot due to pressure loading of the idealized shell structure is illustrated in Figure 4.1. This shows how the stress varies for parametric angles between  $0^\circ$  and  $90^\circ$ . The observed trend correlates with the behaviour of shell structure in transmitting load by ‘membrane’ stresses. These act parallel to the tangential plane at a given point of the middle surface. They are distributed uniformly over the shell’s thickness.

The strain contour plot (Figure 4.2) also agrees with the stress distribution. Figures 4.3 and 4.4 illustrate the variations of the tangential and radial strains, respectively. The tangential strain plot shows a repeated trend of dwelling and increasing from  $0^\circ$  to  $90^\circ$ , while the radial strain plot slopes upward, from left to right, increasing gradually from  $0^\circ$  to  $90^\circ$ .

The contour plot of the deformations shows a variation between the radial and tangential deformations. The tangential deformation (Figure 4.6) jump start and then gradually increases as  $\varphi$  approaches  $90^\circ$ . The radial deformation, however, shows a parabolic trend. It peaked at  $\varphi = 40^\circ$  and gradually drops to zero. The possible reasons for the results presented in this section will be discussed in section 4.43.

#### **4.42 Computational Finite Element Model**

The results of the 2-D finite element model validate the analytical results presented in Section 4.41. The stress distribution due to the applied pressure load is shown in Figures 4.9 and 4.10. Note the difference between the deformed and undeformed mesh plots. This shows how the stress varies for parametric angles between  $0^\circ$  and  $90^\circ$ . Again, the observed trend correlates with the behaviour of shell structure in transmitting load by ‘membrane’ stresses, as shown by the analytical model results (Section 4.41).

The results of the 3-D finite element models are shown in Figures 4.13 to 4.15. The stress response of the dome structure is shown in Figure 4.13. There is stress concentration round the edge of the dome for both the single layer and the multilayer dome structure. There is a marked difference between the deformed single layer model and the multilayer counterpart (Figures 4.14 and 4.15).

#### **4.43 Discussion**

A simple analytical model and a 2-D finite element model was used to simulate the behaviour of Ke tortoise shell under the compressive action of pressure load as form of broad load. The degree to which this model agrees with natural loading depends on how tortoises are naturally stressed in the wild. Real-world forces may be similar to the imposed pressure load, but they may act for quite a short duration with more complex geometrical patterns [2]. Nevertheless, the simulations provide some insight into how the multilayered structure of the studied biological material (Ke) responds to forces that are applied locally to the shell structure.

The variation of stress along the shell’s surface is such that the stress increases as  $\varphi$  approaches  $90^\circ$ , which corresponds to the point on the shell where the carapace is hinged to the plastron. The geometry at this point tends to be sharp constituting a stress raiser. The radial deformation at this hinge is zero, illustrating further that the shell failure is likely to be initiated at the hinge where both the tangential deformation and stress are maximum and radial deformation is zero. This

gives a potential bioinspired approach to shell structure design that is resistant to deformation at its peak ( $\varphi = 0^\circ$ ).

The stress concentration round the edges of the dome architecture (Figure 4.13) suggests the reason for which the marginal bones that form the edges of Ke tortoise shell are thicker than the remaining sections of the shell. This allows the shell to survive such predatory attacks as from alligator and aves [3].

Considering the stress responses of single layer shell and multilayered shell (Figures 4.14 and 4.15), it can be seen that the distortion in the single layer shell is moderate compared to the multilayered shell.

#### 4.5 Summary

Analytical and computational models of shell structure have been presented in this chapter. The geometry of the shell is shown to have significant effects on its response to applied load. This gives a potential bioinspired approach to shell structure design that is resistant to deformation at its peak ( $\varphi = 0^\circ$ ).

#### References

1. **Stephen T. and Woinowsky-Krieger S.** *Theory of Plates and Shells*. Singapore : McGraw-Hill, Inc., 1959. 0-07-085820-9.
2. **Magwene, P. M., Socha, J. J.** *Biomechanics of turtle shells: How whole shells fail in compression*. 2012. J. Exp. Zool. 9999A:1 – 13.
3. **Magwene, P. M., Socha, J. J.** *Biomechanics of turtle shells: How whole shells fail in compression*. 2012. J. Exp. Zool. 9999A:1 – 13.

$\varphi^\circ$	$N_\varphi$ (N/m) $\times 10^4$	$N_\theta$ (N/m) $\times 10^4$	$\epsilon_\varphi \times 10^{-3}$	$\epsilon_\theta$	$v$ (m) $\times 10^{-8}$	$w$ (m) $\times 10^{-3}$
0	-2.5433	-5.0800	-0.6773	-0.0033	0.2908	0.0677
10	-2.5516	-5.0966	-0.6795	-0.0033	0.4028	0.1697
20	-2.5762	-5.1455	-0.6861	-0.0034	0.5697	0.1729
30	-2.6154	-5.2231	-0.6967	-0.0034	0.6399	0.1782
40	-2.6658	-5.3234	-0.7103	-0.0035	0.6413	0.1851
50	-2.7229	-5.4366	-0.7257	-0.0035	0.5869	0.1931
60	-2.7801	-5.5498	-0.7411	-0.0036	0.4857	0.2012
70	-2.8294	-5.6476	-0.7544	-0.0037	0.3467	0.2084
80	-2.8630	-5.7142	-0.7636	-0.0037	0.1805	0.2134
90	-2.8750	-5.7379	-0.7668	-0.0037	0.0000	0.2151

Table 4.1: Analytical solutions based on theory of shell

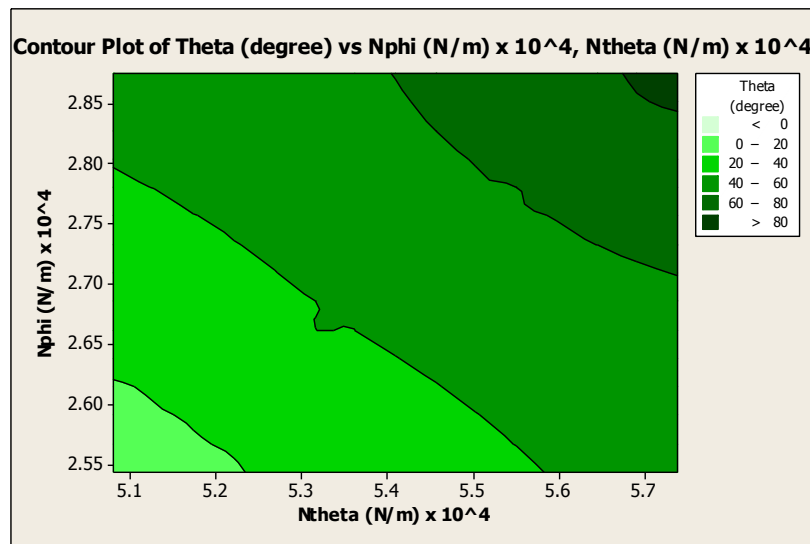


Figure 4.1: Stress distribution along the surface of the shell

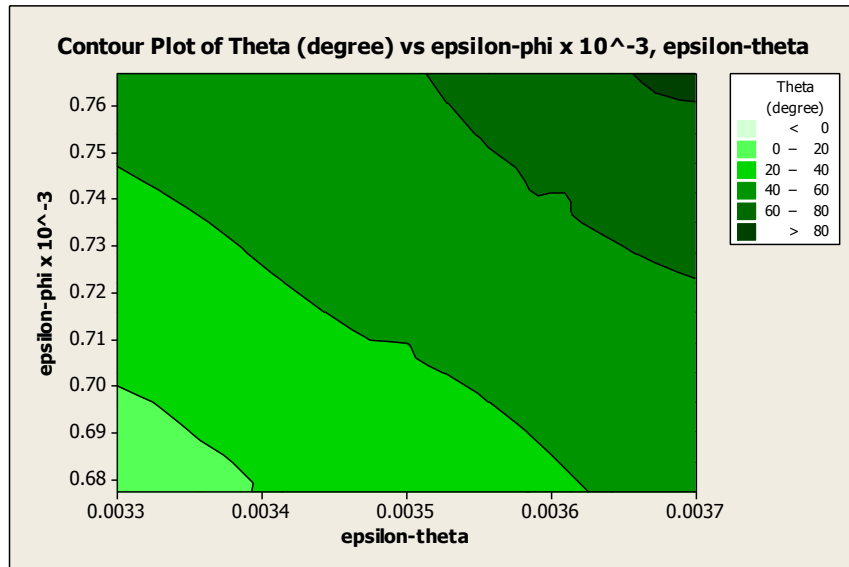


Figure 4.2: Strain distribution along the surface of the shell

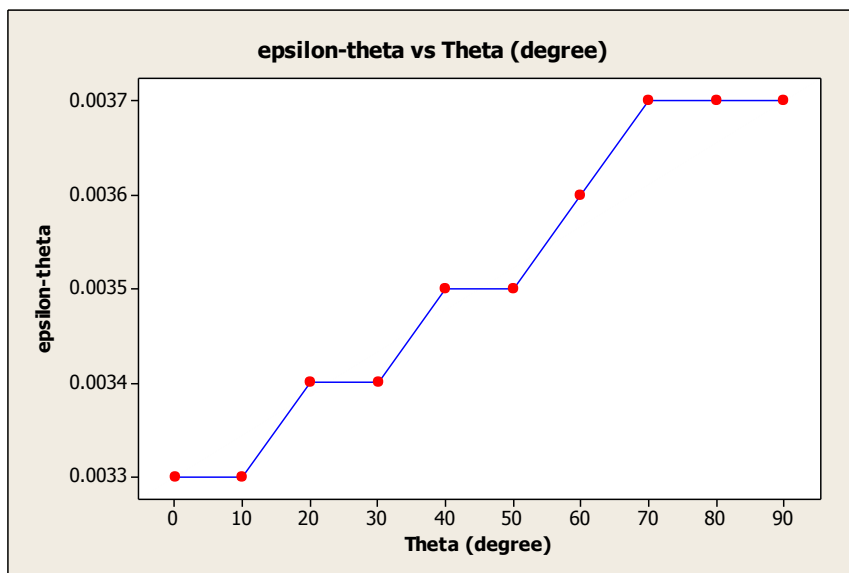


Figure 4.3: Tangential strain distribution along the surface of the shell

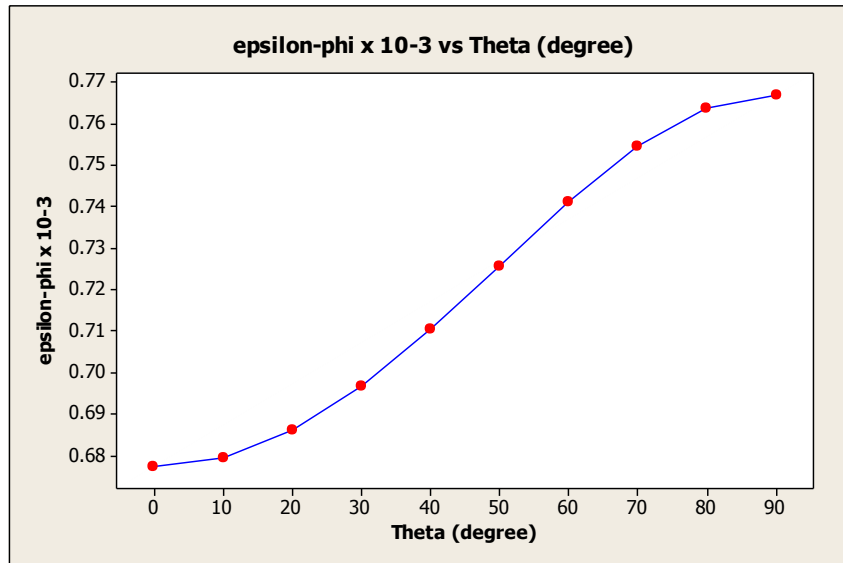


Figure 4.4: Radial strain distribution along the surface of the shell

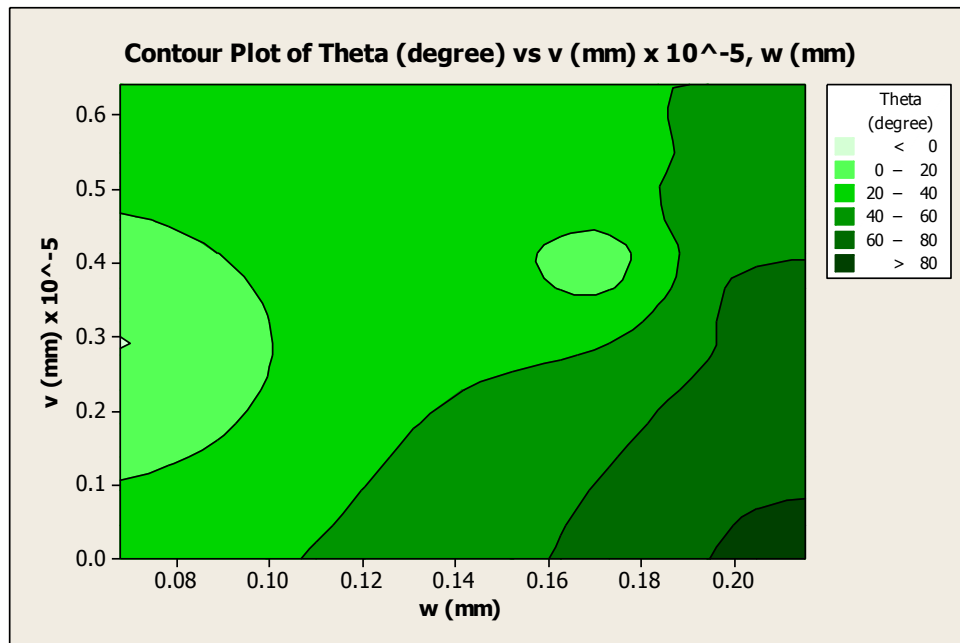


Figure 4.5: Deformation distribution along the surface of the shell

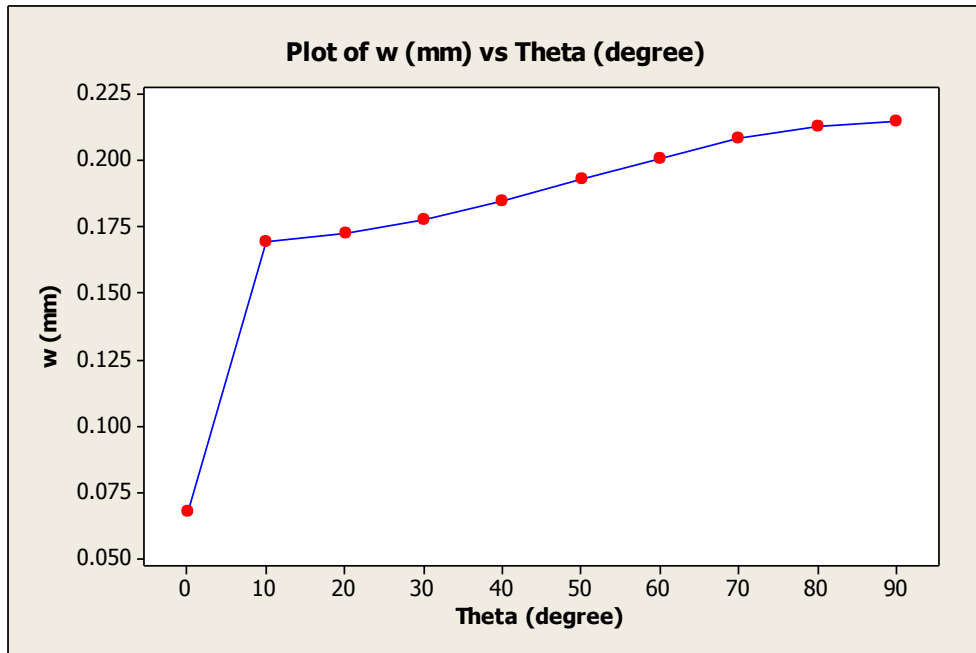


Figure 4.6: Tangential deformation distribution along the surface of the shell

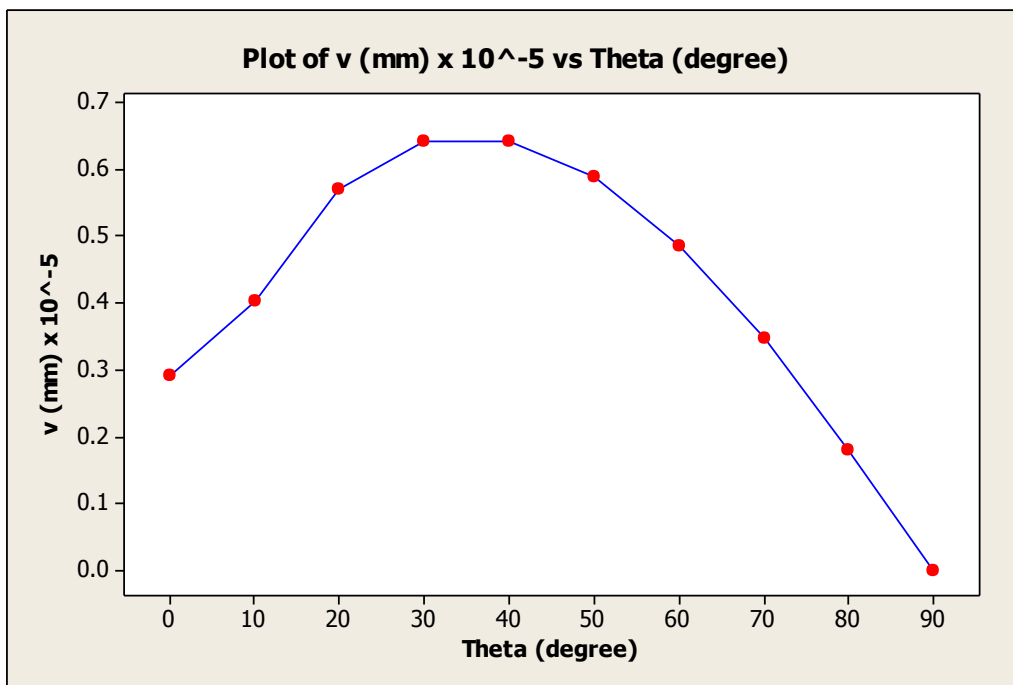


Figure 4.7: Radial deformation distribution along the surface of the shell

	Single layer shell
Element type	CPS4R
Number of elements	715
Number of nodes	955
Number of degrees of freedom (DOF)	1,910

Table 4.2: 2-D Finite element simulation conditions

	Single Layer Dome	Multilayer Dome
Element type	S4R	S4R
Number of elements	775	880
Number of nodes	765	882
Number of degrees of freedom (DOF)	4590	5292

Table 4.3: 3-D Finite element simulation conditions

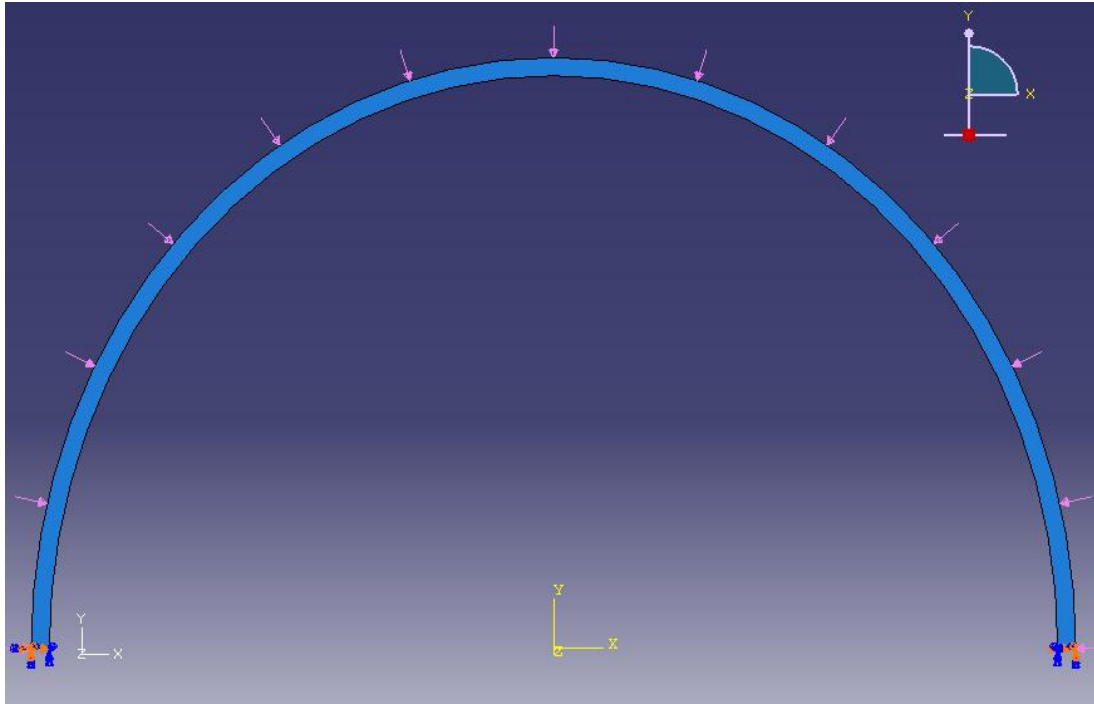


Figure 4.8: Loaded 2-D finite element model of the shell structure

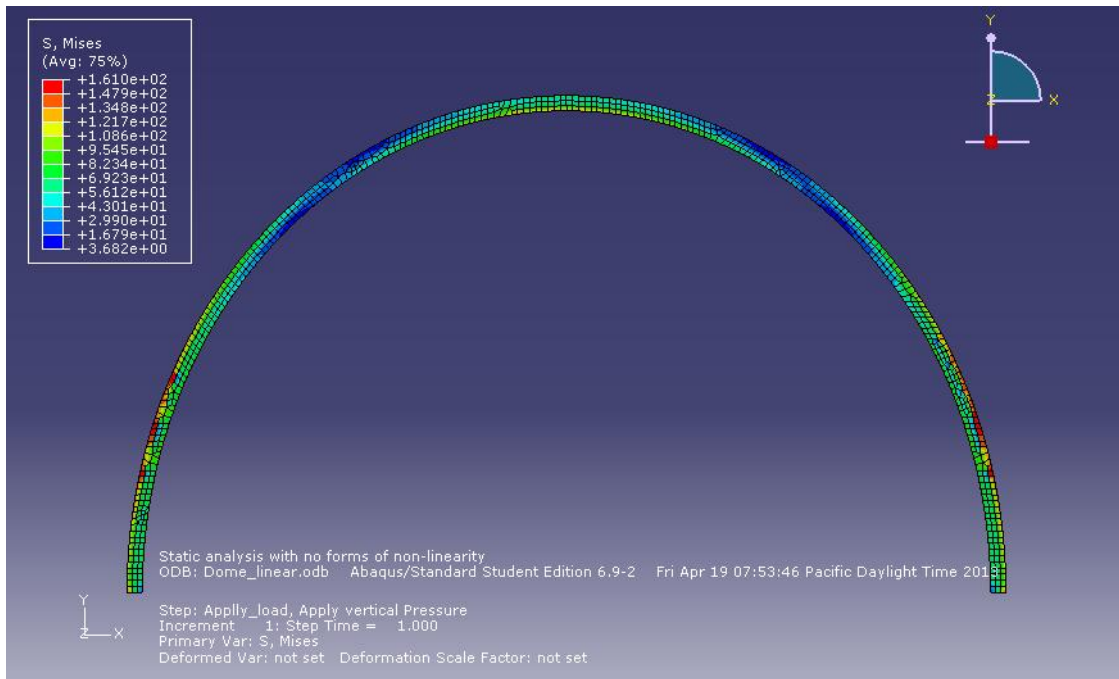


Figure 4.9: 2-D Finite element model showing stress distribution along the surface of the shell (undeformed)

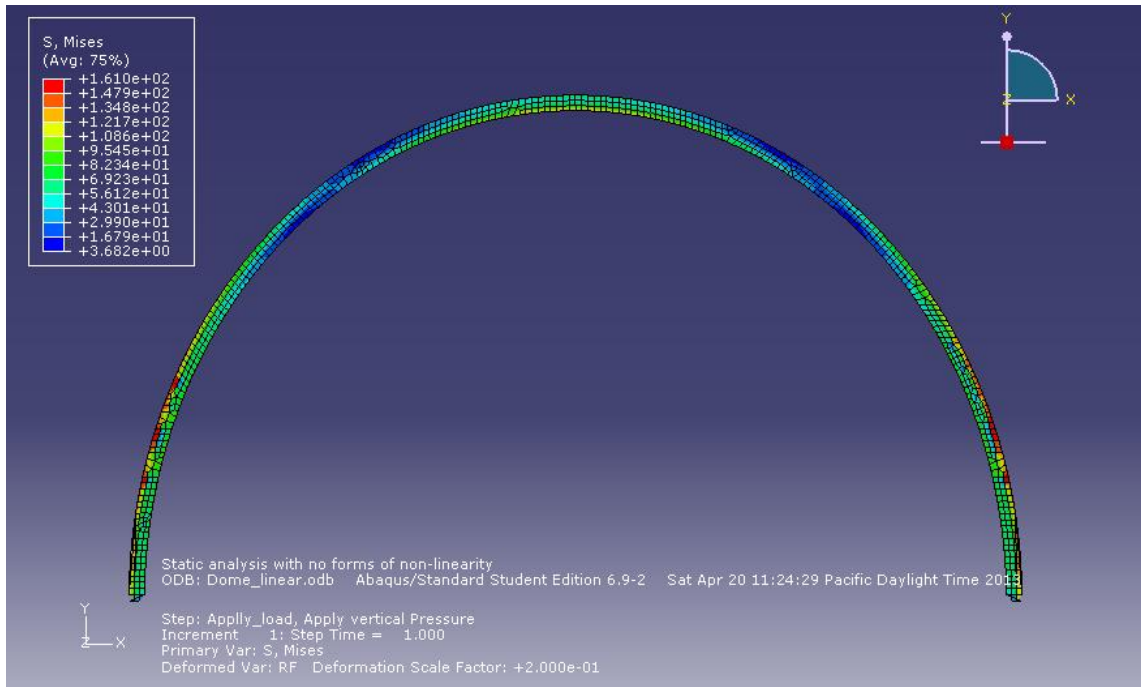


Figure 4.10: 2-D Finite element model showing stress distribution along the surface of the shell (deformed)

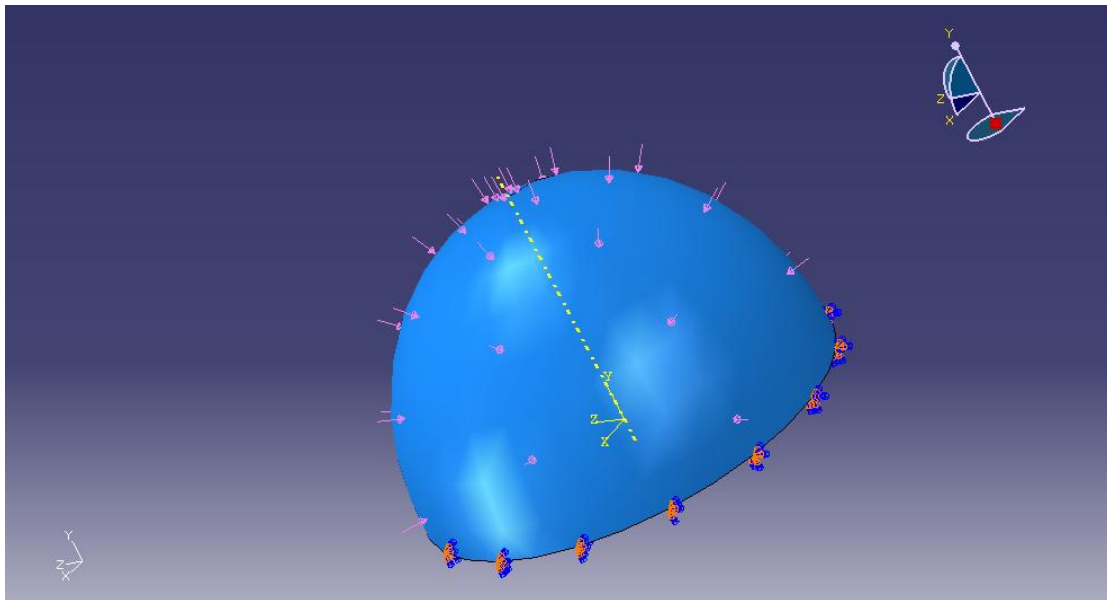


Figure 4.11: Loaded 3-D finite element model of the dome structure

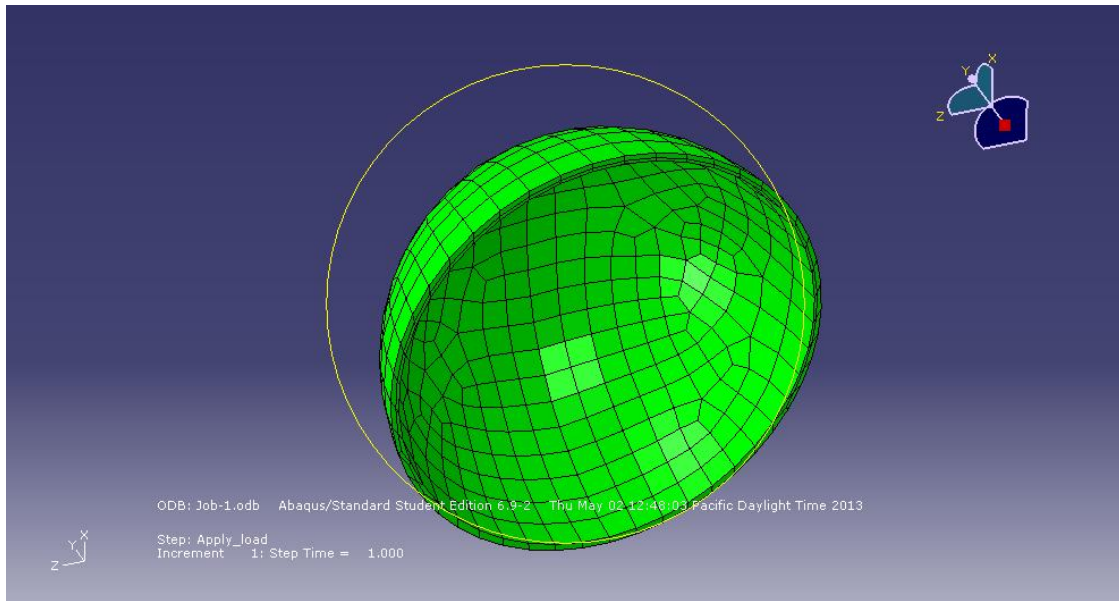


Figure 4.12: Meshed 3-D finite element model of the dome structure (undeformed)

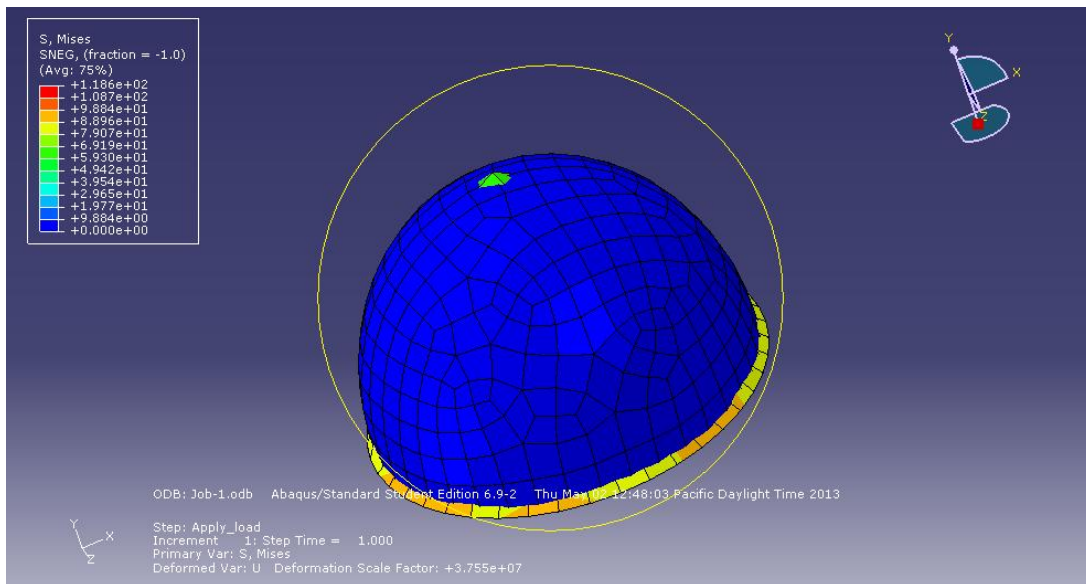


Figure 4.13: 3-D Finite element model showing stress distribution on the surface of the dome structure (deformed single/multilayer)

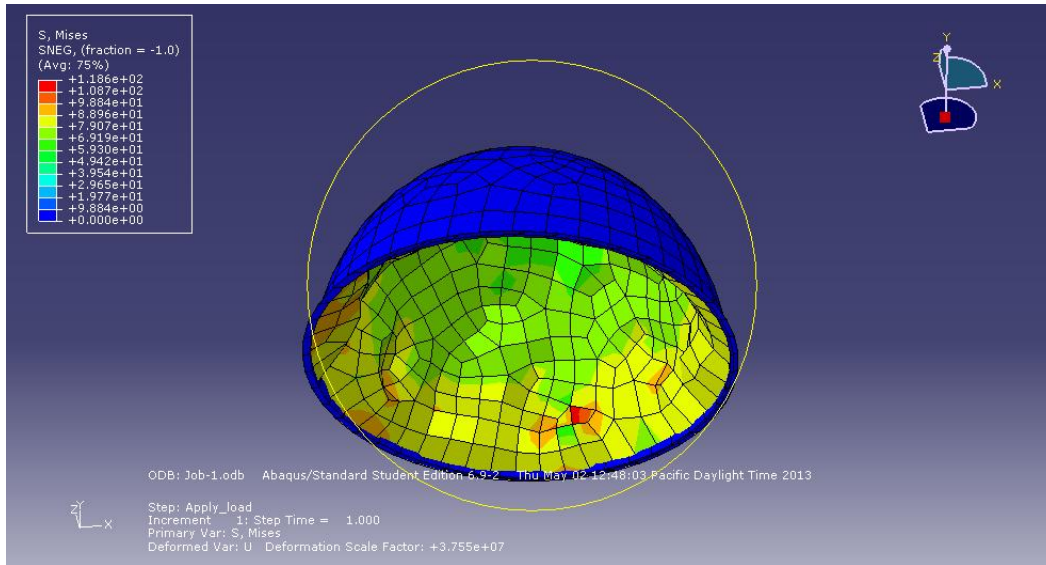


Figure 4.14: 3-D Finite element model showing stress distribution on the surface of the dome structure (deformed multilayer)

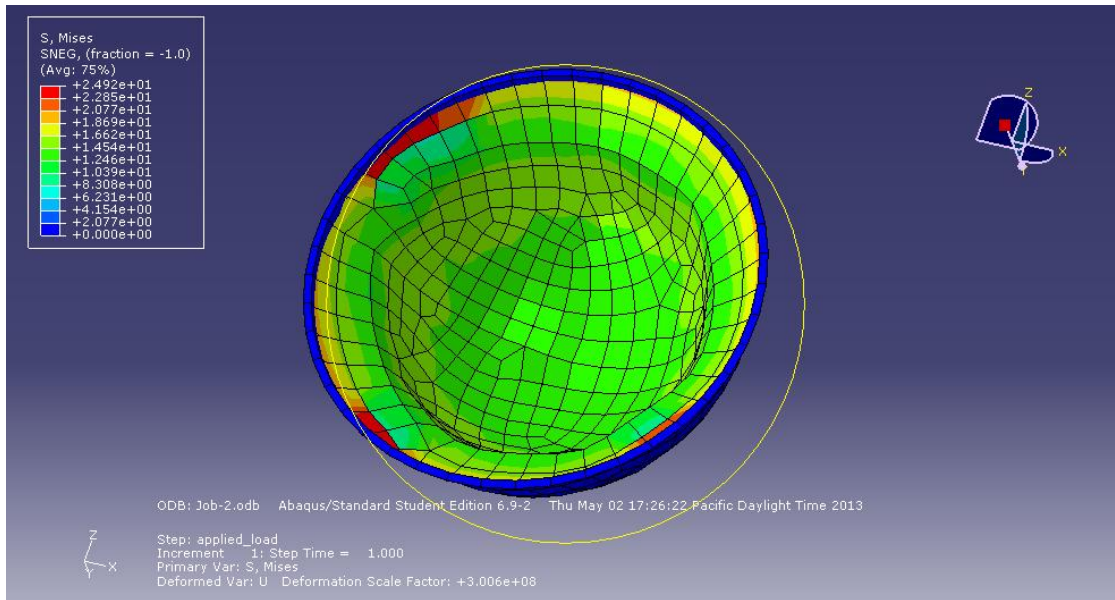


Figure 4.15: 3-D Finite element model showing stress distribution on the surface of the dome structure (deformed single layer)

## **5.0 Concluding Remarks and Suggested Future Work**

### **5.1 Summary and Concluding Remarks**

In this work, a combination of experiment, analytical and computational model has been used to investigate the deformation and stress responses of a *Kinixys erosa* tortoise shell structure as a potential source of inspiration for the design of a failure resistant shell/layered structure. The experiments gave the material properties that were used in the analytical and computational models. Salient conclusions arising from this study are summarized below:

- a) The carapace of *Kinixys erosa* (Ke) is a sandwich composite structure with a denser exterior lamellar bone layers (cortical bone) and an interior bony network of closed-cell fibrous foam layer (cancellous bone).
- b) The scute of *Kinixys erosa* (Ke) was found to be resistant to concentrated acid and base.
- c) The analytical and computational models showed that the geometry of a shell structure has significant effects on its deformation and stress responses.
- d) The computational models showed that shell architecture vis-a-vis single layer and multilayer has significant effects on its deformation and stress responses.
- e) This work introduces the use of shell theory [1] in studying the deformation and stress responses of tortoise shell.

### **5.2 Implications and Possible Bioinspired Applications**

The implications of the above salient conclusions are quite significant in understanding why nature made the *Ke erosa* tortoise shell multilayered varying section thickness. Some of the implications and possible bioinspired applications are stated below:

- The *Ke erosa* tortoise shell is highly adapted to bending stress distribution in a way that the regions subjected to high stresses are denser (lower and outer layers) compare to the middle layer where stresses are low.

- The density gradation from outer to inner layer allows for energy absorption in a case of impact loading.
- The chemical resistance of the outer scute layer is able to protect the tortoise from environmental hazards like acid rain resulting from air pollutions.
- These implications provides potential for bioinspired design of **multilayered armour clothing** with a stiff outer and lower layers and cellular inner layer capable of dissipating impact energy, in a way that gives overall protection from the impact force.
- They also provide bioinspiration for the design of **multilayered dome structure** with an impervious stiff outer layer without interconnected pores that provides environmental protection to the entire structure, and a core that structurally provides continuous support for the outer layer.

### 5.3 Suggestions for Future Work

#### 5.31 Microstructural and compositional characterization of *Kinixys erosa* (Ke) carapace materials

In addition to the optical microscopy and XRD, SEM and EDX study of Ke carapace materials will provide more insight into the microstructure and composition of Ke tortoise shell.

#### 5.32 Mechanical characterization of *Kinixys erosa* (Ke) carapace materials

Nanoindentation technique will be used to measure the modulus of the individual layer of Ke tortoise shell carapace, to be used in:

- a) Object oriented finite element (OOF2) [2] analysis to estimate the effective modulus of the carapace. The modulus ( $E_B$ ) obtained from the bending test and the OOF2 can then be compared.
- b) Modeling of a multilayered-shell and layered structures to understand their deformation and stress responses.

## References

1. **Stephen T. and Woinowsky-Krieger S.** *Theory of Plates and Shells*. Singapore : McGraw-Hill, Inc., 1959. 0-07-085820-9.
2. **Kantesh, B., Riken, R. P., Anup, K. K., Debrupa, L., Arvind, A.** *Multi-scale hierarchy of Chelydra serpentina: Microstructure and mechanical properties of turtle shell*. s.l. : Elsevier, 2011, *Journal of the Mechanical Behavior of Biomedical Materials*, Vol. 4, pp. 1440-1451.

## APPENDIX A

### Analytical Solution of Shell Behaviour under Pressure load Based on Theory of Shell

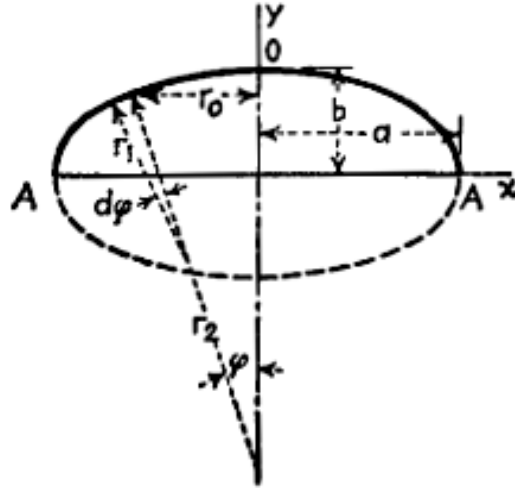


Figure 1: Shell in the form of ellipsoid revolution

Figure 1 depicts the ellipsoid used to analyse the behaviour of the Ke tortoise shell under a pressure load, assuming symmetry. Reference to the ventral/dorsal view of Ke tortoise shell  $a$  and  $b$  represents the minor radius and the ellipsoidal dome height respectively.  $r_0$  is the radius of the cross-section of the parallel circle described by the applied pressure load  $p$  a form of broad load.  $r_1$  and  $r_2$  are the principal radii of curvature.  $\varphi$  is the distribution angle as the stress, strain, and deflection varies from O to the equator AA. For a shell problem the stress is often taken as force per length, in this case,  $N_\varphi$  and  $N_\theta$ .  $\epsilon_\varphi$  and  $\epsilon_\theta$  are the radial and tangential strains respectively.

$$r_0 = r_2 \sin \varphi \dots\dots\dots (1)$$

$$r_1 = \frac{a^2 b^2}{(a^2 \sin^2 \varphi + b^2 \cos^2 \varphi)^{\frac{3}{2}}} \dots\dots\dots (2)$$

$$r_2 = \frac{a^2}{(a^2 \sin^2 \varphi + b^2 \cos^2 \varphi)^{\frac{1}{2}}} \dots\dots\dots (3)$$

For a shell problem the stress distribution is often taken as force per length, in this case,  $N_\varphi$  and  $N_\theta$ . If the resultant of the load on the shell is  $\mathbf{R}$ , the equilibrium equation is given as:

$$2\pi r_0 N_\varphi \sin \varphi + R = 0 \dots \dots \dots (4), \text{ which implies}$$

$$N_\varphi = \frac{-R}{2\pi r_0 \sin \varphi} \dots \dots \dots (5)$$

Where  $R = p\pi r_0^2$

$N_\theta$  can therefore be obtained by inserting  $N_\varphi$ ,  $r_1$ , and  $r_2$  into (6) and taking  $Z = p$ :

$$\frac{N_\varphi}{r_1} + \frac{N_\theta}{r_2} = -Z \dots \dots \dots (6)$$

Hence,

$$N_\varphi = \frac{-pr_2}{2} \text{ and } N_\theta = pr_2 \left( \frac{r_2}{2r_1} - 1 \right) \dots \dots \dots (7)$$

It could be recalled that for an isotropic problem (invoking Hooke's law) the tangential and normal strain  $\epsilon_\varphi$  and  $\epsilon_\theta$  respectively can be written as:

$$\epsilon_\varphi = \frac{1}{Eh} (N_\varphi - \nu N_\theta) \text{ and } \epsilon_\theta = \frac{1}{Eh} (N_\theta - \nu N_\varphi) \dots \dots \dots (8)$$

Considering a symmetrical deformation, a small displacement of a point can be resolved into  $v$  and  $w$  in the direction of tangent to the meridian and normal direction to the middle surface respectively.

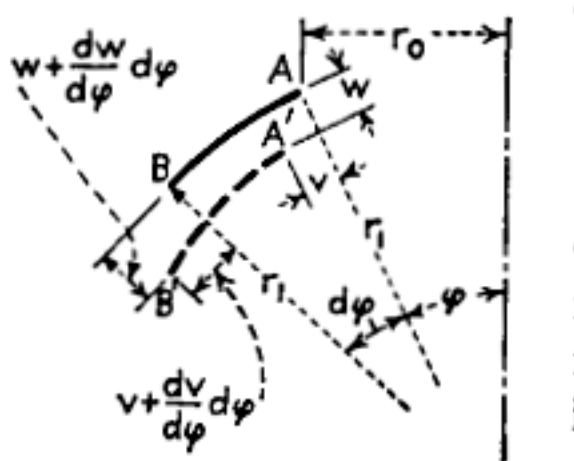


Figure 2: A meridional element showing the displacement of symmetrically loaded shell.

Taking an element AB as shown in Figure 2 above, the increase in length of the element due to tangential displacements  $v$  and  $v + (dv/d\varphi)d\varphi$  of its equal ends is equal to  $(dv/d\varphi)d\varphi$ . Because of the radial displacement  $w$  of the points A and B the length of the element decreases by an amount  $w d\varphi$ . Neglecting the change in length due to the difference in the radial displacement of the points A and B as a small quantity of higher order, the effective change in length of the element AB due to deformation is given as

$$\Delta l = \left(\frac{dv}{d\varphi}\right) d\varphi - w d\varphi$$

If the initial length ( $l_0$ ) is  $r_1 d\varphi$  then

$$\epsilon = \frac{\Delta l}{l_0}$$

can be expressed as

$$\epsilon_\varphi = \frac{\left(\frac{dv}{d\varphi}\right) d\varphi - w d\varphi}{r_1 d\varphi} = \frac{1}{r_1} \frac{dv}{d\varphi} - \frac{w}{r_1}$$

$$\therefore \epsilon_\varphi = \frac{1}{r_1} \frac{dv}{d\varphi} - \frac{w}{r_1} \dots \dots \dots (a)$$

However, considering an element of a parallel circle of radius  $r_0$  it can be seen (Figure 2) that due to displacements  $v$  and  $w$  the radius of the circle increases by an amount

$$\Delta r = v \cos \varphi - w \sin \varphi$$

The circumference of the circle also increases in the same proportion as the radius, thus;

$$\epsilon_\theta = \frac{\Delta r}{r_0} = \frac{1}{r_0} (v \cos \varphi - w \sin \varphi)$$

But  $r_0 = r_2 \sin \varphi$

$$\therefore \epsilon_\theta = \frac{1}{r_2} (v \cot \varphi - w) \dots \dots \dots (b)$$

Combining equations (8), (a), and (b) yields:

$$\epsilon_\varphi = \frac{1}{r_1} \frac{dv}{d\varphi} - \frac{w}{r_1} = \frac{1}{Eh} (N_\varphi - vN_\theta)$$

$$\epsilon_\theta = \frac{1}{r_2} (v \cot \varphi - w) = \frac{1}{Eh} (N_\theta - vN_\varphi)$$

But

$$N_\varphi = \frac{-pr_2}{2} \text{ and } N_\theta = pr_2 \left( \frac{r_2}{2r_1} - 1 \right)$$

Therefore

$$\frac{dv}{d\varphi} - w = \frac{pr_1r_2}{Eh} \left[ v \left( 1 - \frac{r_2}{2r_1} \right) - \frac{1}{2} \right] \dots \dots \dots (c)$$

$$v \cot \varphi - w = \frac{pr_2^2}{Eh} \left[ \left( \frac{r_2}{2r_1} - 1 \right) + \frac{v}{2} \right] \dots \dots \dots (d)$$

Subtracting (d) from (c) gives

$$\frac{dv}{d\varphi} - v \cot \varphi = \frac{pr_1r_2}{Eh} \left[ v \left( 1 - \frac{r_2}{2r_1} \right) - \frac{1}{2} \right] - \frac{pr_2^2}{Eh} \left[ \left( \frac{r_2}{2r_1} - 1 \right) + \frac{v}{2} \right] \dots \dots \dots (e)$$

If the right hand side of (e) is taken as  $y$ , then

$$\frac{dv}{d\varphi} = v \cot \varphi + y \dots \dots \dots (i)$$

This is a first order differential equation.

Let

$$\frac{dv}{d\varphi} = v \cot \varphi \text{ homogenous part } \dots \dots \dots (ii)$$

Assume a solution of the form

$$v = Ce^{P(\varphi)}$$

$$P(\varphi) = \int P d\varphi, \quad P = \cot \varphi$$

$$P(\varphi) = \int \cot \varphi \, d\varphi = \ln \sin \varphi$$

$$v = Ce^{\ln \sin \varphi} = C \sin \varphi$$

Therefore a solution of the form  $v = C(\varphi) \sin \varphi$  can be assumed for (i), such that

$$\frac{dv}{d\varphi} = C(\varphi) \cos \varphi + \cos' \varphi \sin \varphi$$

Then we can write

$$C(\varphi) \cos \varphi + \cos' \varphi \sin \varphi = C \sin \varphi \cot \varphi + y$$

Therefore

$$\cos' \varphi \sin \varphi = y$$

This implies

$$C(\varphi) = y \int \frac{d\varphi}{\sin \varphi} \dots \dots \dots \text{(iii)}$$

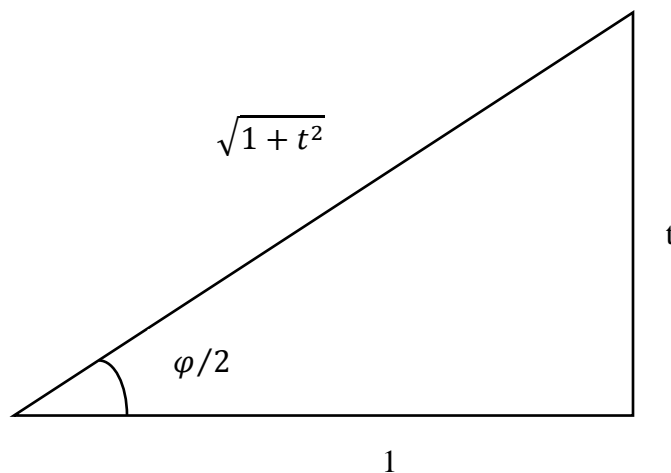
Let

$$\tan \frac{\varphi}{2} = t$$

Such that

$$\varphi = 2 \tan^{-1} t$$

$$d\varphi = \frac{2}{1+t^2} dt \dots \dots \dots (*')$$



Also

$$\sin \varphi = 2 \sin \frac{\varphi}{2} \cos \frac{\varphi}{2}$$

$$\sin \varphi = \frac{2t}{1+t^2} \dots \dots \dots (*'')$$

Inserting  $d\varphi$  and  $\sin\varphi$  into (iii) gives

$$C(\varphi) = y \int \frac{2}{1+t^2} dt \left( \frac{2t}{1+t^2} \right)^{-1}$$

$$C(\varphi) = y \int \frac{dt}{t} = y \ln t + K, \text{ where } K = \text{integration constant}$$

$$C(\varphi) = y \ln \left( \tan \frac{\varphi}{2} \right) + K$$

Therefore the solution of (I) can be written as

$$v(\varphi) = y \ln \left( \tan \frac{\varphi}{2} \right) \sin \varphi + K$$

Imposing the BC:

$$\text{at } \varphi = \frac{\pi}{2} \quad v(\varphi) = 0$$

implies  $K=0$

Therefore

$$v(\varphi) = y \ln \left( \tan \frac{\varphi}{2} \right) \sin \varphi \dots \dots \dots (I)$$

$w(\varphi)$  can be obtained from (d) by substituting  $v(\varphi)$  thus

$$w = v \cot \varphi - \frac{pr_2^2}{Eh} \left[ \left( \frac{r_2}{2r_1} - 1 \right) + \frac{v}{2} \right]$$

$$w = y \ln \left( \tan \frac{\varphi}{2} \right) \sin \varphi \cot \varphi - \frac{pr_2^2}{Eh} \left[ \left( \frac{r_2}{2r_1} - 1 \right) + \frac{v}{2} \right]$$

$$w = y \ln \left( \tan \frac{\varphi}{2} \right) \cos \varphi - \frac{pr_2^2}{Eh} \left[ \left( \frac{r_2}{2r_1} - 1 \right) + \frac{v}{2} \right] \dots \dots \dots (II)$$

## APPENDIX B

### Matlab code for analytical solution of monolayer ellipsoidal shell

```
%%% Stresses %%%
a = 0.0575; b = 0.065; phi = [0:10:90];
P = 1*10^6;
r1 = (a*b)^2./((a*sin((pi/180).*phi)).^2 +
(b*cos((pi/180).*phi)).^2).^1.5;
r2 = a^2./((a*sin((pi/180).*phi)).^2 +
(b*cos((pi/180).*phi)).^2).^0.5;
Nphi = -(P.*r2)/2;
Ntheta = P.*r2.*((r2./2.*r1)-1);
%%%%%%%%%%%%%%%%%%%%%%%%%%%%%%%%%%%%%%%%%%%%%%%%%%%%%%%%%%%%%%%%%%%%%%%%
%%% Deflection %%%
E = 6.4 *10^9; u = 0.33; h = 0.002;
x = r1.*u.*(1-(r2./2.*r1)) - 0.5;
z = r2.*((r2./2.*r1)-1) + u/2;
y = (P.*r2./E*h).*(x - z);
v = y.*log(tan((pi/180).*phi/2)).*sin((pi/180).*phi);
w = y.*log(tan((pi/180).*phi/2)).*cos((pi/180).*phi) -
((P.*r2.^2)./(E*h)).*(((r2./2.*r1)-1) + u/2);
%%%%%%%%%%%%%%%%%%%%%%%%%%%%%%%%%%%%%%%%%%%%%%%%%%%%%%%%%%%%%%%%%%%%%%%%
%%%%%%%%%%%%%%%%%%%%%%%%%%%%%%%%%%%%%%%%%%%%%%%%%%%%%%%%%%%%%%%%%%%%%%%%
%%% Strains %%%
etaphi = (Nphi - u*Ntheta)./(E*h);
etatheta = (Ntheta - u*Nphi)./(E*h);
%%%%%%%%%%%%%%%%%%%%%%%%%%%%%%%%%%%%%%%%%%%%%%%%%%%%%%%%%%%%%%%%%%%%%%%%
%% plots %%%
plot(etaphi, Nphi);
```